A Top-Down Pathway to Secondary Eyewall Formation in Simulated Tropical Cyclones

Bryce Tyner[1,2] (iD) **, Ping Zhu[1,2]** (iD) **, Jun A. Zhang[3,4], Sundararaman Gopalakrishnan[4], Frank Marks Jr.[4]** (iD) **, and Vijay Tallapragada[5]** (iD)

[1]International Hurricane Research Center, Miami, FL, USA, [2]Department of Earth and Environment, Florida International University, Miami, FL, USA, [3]Cooperative Institute for Marine and Atmospheric Studies, University of Miami, Miami, FL, USA, [4]Hurricane Research Division, Atlantic Oceanographic and Meteorological Laboratory, NOAA, Miami, FL, USA, [5]Environmental Modeling Center, National Centers for Environmental Prediction, NOAA, Washington, DC, USA

Abstract Idealized and real-case simulations conducted using the Hurricane Weather Research and Forecasting (HWRF) model demonstrate a "top-down" pathway to secondary eyewall formation (SEF) for tropical cyclones (TCs). For the real-case simulations of Hurricane Rita (2005) and Hurricane Edouard (2014), a comparison to observations reveals the timing and overall characteristics of the simulated SEF appear realistic. An important control of the top-down pathway to SEF is the amount and radial-height distribution of hydrometeors at outer radii. Examination into the simulated hydrometeor particle fall speed distribution reveals that the HWRF operational microphysics scheme is not producing the lightest hydrometeors, which are likely present in observed TCs and are most conducive to being advected from the primary eyewall to the outer rainband region of the TC. Triggering of SEF begins with the fallout of hydrometeors at the outer radii from the TC primary eyewall, where penetrative downdrafts resulting from evaporative cooling of precipitation promote the development of local convection. As the convection-induced radial convergence that is initially located in the midtroposphere extends downward into the boundary layer, it results in the eruption of high entropy air out of the boundary layer. This leads to the rapid development of rainband convection and subsequent SEF via a positive feedback among precipitation, convection, and boundary layer processes.

1. Introduction

Producing timely and accurate tropical cyclone (TC) forecasts remains one of the most difficult challenges facing meteorologists today. Improvements in TC track forecasts over recent decades have correlated well with improvements in numerical weather prediction because TC track is largely dictated by the resolved, large-scale environmental flow. In contrast, TC intensity forecasts have not shown similar improvement, evidence that TC intensity at a given time is also dictated by TC internal dynamics involving subgrid-scale (SGS) processes that must be parameterized. A number of studies have revealed the importance of these internal SGS processes and how they interact with the resolved aspects of the TC to ultimately determine TC inner-core structure and intensity (e.g., Abarca & Montgomery, 2013; Menelaou et al., 2014; Zhang et al., 2017; Zhu & Zhu, 2014, 2015).

Secondary eyewall formation (SEF) and the ensuing eyewall replacement cycle (ERC) are frequently observed in intense TCs (e.g., Didlake & Houze, 2011; Houze et al., 2007; Kossin & Sitkowski, 2009; Willoughby et al., 1982). Based on a 10 year data set of passive microwave satellite imagery, Hawkins and Helveston (2008) showed that more than 50% of all TCs that reach an intensity of 120 kt have multiple eyewalls present during their lifespan. The SEF and ERC can result in a rapid change in TC structure and intensity, and thus, timely prediction of these features is of great interest to forecasters. The ERC is typically associated with a temporary weakening in overall TC intensity but also an increase in the radial extent of damaging wind speeds. In contrast to the frequency of observed ERCs in intense TCs, operational models often fail to produce secondary eyewalls (Abarca & Montgomery, 2013). Even when numerical models are able to produce ERCs, the simulated ERCs often do not match the timing and characteristics of the observed cases (Fierro et al., 2009). This failure of operational models in spite of capturing the large-scale environment suggests that TC internal dynamics are not being properly captured in these models.

Following the pioneering work of Eliassen (1951), Shapiro and Willoughby (1982) calculated the balanced, transverse response to local sources of momentum and heat at various heights and distances from the

radius of maximum wind (RMW) in axisymmetric TCs. When a heat source was introduced in the lower troposphere outside of the RMW, their Sawyer-Eliassen diagnoses showed that there was a positive tangential wind tendency in the region between the RMW and the local heat source. If the heat source persisted for enough time, a secondary tangential wind maximum could form. This result suggests that diabatic heating outside the RMW is essential to SEF. In a more recent work, using full-physics-idealized simulations from the Weather Research and Forecasting (WRF) model as well as a linearized axisymmetric nonhydrostatic model, Rozoff et al. (2012) reevaluated the symmetric balanced explanation of SEF provided by Shapiro and Willoughby (1982). Their analyses confirmed that the persistent diabatic heating outside the primary eyewall was responsible for the broadening of the wind field and the eventual occurrence of SEF. The role of diabatic heating outside of the primary eyewall in driving SEF and outer rainbands from a symmetric balanced perspective has also been supported by Wang (2009), Judt and Chen (2010), Moon and Nolan (2010), and Zhu and Zhu (2014).

Using a two-dimensional nondivergent model, Montgomery and Kallenbach (1997) provided a pure dynamical explanation for how diabatic heating outside the RMW can accelerate the vortex mean flow. They showed that asymmetric disturbances resulting from diabatic heating can propagate radially outward in the form of vortex Rossby waves. Due to the radial shearing effect, the wave packets slow down and eventually cease at stagnation radii, where the wave energy is axisymmetrized into the vortex mean flow. Later studies confirmed that this wave-mean-flow interaction from the asymmetric perspective can indeed lead to SEF (e.g., Terwey & Montgomery, 2008; Martinez et al., 2010; Menelaou et al., 2012, 2013).

While the symmetric and asymmetric explanations for SEF differ, both theories recognize the crucial role of diabatic heating outside of the RMW in driving SEF. Given that diabatic heating produced by outer rainband convection almost always exists for a TC, why does SEF only occur at certain periods during the lifecycle of a subset of TCs? A triggering mechanism for SEF needs to be established.

Recent studies have revealed that boundary layer processes could be important for triggering SEF. Huang et al. (2012) first demonstrated the role of unbalanced boundary layer dynamics in triggering SEF using simulations of Typhoon Sinlaku (2008). In this proposed paradigm, SEF begins with a broadening and strengthening of the tangential winds above the boundary layer, resulting from the diabatic heating generated by sporadic convection outside of the eyewall. An increase in frictionally induced radial inflow emerges within the boundary layer along with associated radial advection of momentum. In a narrow region, the radial advection of momentum occurs fast enough to overcome frictional dissipation, resulting in supergradient flow in the region. This supergradient flow causes deceleration of boundary layer inflow, leading to radial flow convergence. The convergence permits the eruption of moist air out of the boundary layer and fosters deep convection in this SEF region. This "bottom-up" pathway to SEF depicted by Huang et al. (2012) was later confirmed by several other studies (e.g., Abarca & Montgomery, 2013, 2014; Qiu & Tan, 2013; Wang et al., 2013).

Kepert (2013) used a number of steady state axisymmetric hurricane boundary layer models to examine the boundary layer response to an imposed radial profile of tangential winds with two wind maxima. Based on the results of his study, he proposed a positive feedback mechanism among local enhancement of the radial vorticity gradient, the frictional updraft, and convection for SEF, which is different from the SEF pathway depicted by Huang et al. (2012). Because of the steady state, axisymmetric nature of the models used in the study, he argued that supergradient flow is not essential to SEF, although the presence of supergradient flow could affect the details of the frictionally forced updraft. While it remains a heated debate on the details of how the boundary layer contributes to SEF and ERC in TCs (Kepert & Nolan, 2014; Montgomery et al., 2014), all of these studies are in agreement that boundary layer processes serve as the important triggering mechanism for SEF.

The question remains: why do models often fail to accurately produce secondary eyewalls? Perhaps boundary layer turbulent processes in the TC inner-core region are not being well represented in the models, resulting in the failure to produce the appropriate triggering for SEF. However, recent ongoing research on the TC boundary layer has yet to identify any major issue of boundary layer parameterization that may prevent SEF triggering (e.g., Zhang et al., 2015; Zhu & Zhu, 2015). Alternatively, perhaps the failure of models can be attributed to other triggering mechanisms for SEF that have not been fully explored and appropriately captured by

the models. Due to its close ties to diabatic heating, the potential role of microphysics in triggering SEF is worth investigating.

Using simulations from the Hurricane Weather Research and Forecasting (HWRF) model, Zhu et al. (2015) showed that the lack of solid-phase hydrometeors and evaporative cooling from precipitation in the outer rainband region are the likely culprits for not generating SEF. Zhu and Zhu (2015) demonstrated that changing the snow terminal velocity by various factors directly led to the presence or absence of SEF in the Advanced Research Weather Research and Forecasting (WRF-ARW) model. While the impact of microphysics on SEF is evident from these studies, the possible triggering mechanism of SEF by microphysical processes has yet to be addressed. Zhang et al. (2016) analyzed composites of five ensemble members with similar SEF characteristics from an ensemble of WRF-ARW simulations along with diagnoses from a boundary layer model. Their analyses showed that while boundary layer processes are important in determining the characteristics of SEF, the SEF shown in the composites was not initiated in the boundary layer, but rather originated in the upper levels. The results suggested a potential different triggering mechanism for SEF other than the bottom-up pathway initiated within the boundary layer.

In the current study, we first explore why the observed SEFs in Hurricane Rita (2005) and Edouard (2014) are poorly reproduced by the operational HWRF model. Based on the finding, we further use sensitivity experiments of both idealized and real-case simulations of HWRF to demonstrate a "top-down" pathway to SEF triggered by a microphysical process, which likely occurred in Hurricane Rita (2005) and Edouard (2014). The manuscript is as organized as follows. Section 2 provides a brief description of HWRF model configuration, construction of an idealized TC vortex, and real TC cases used in this study. The justification for and the design of sensitivity experiments is also described in this section. The results of the idealized experiments are shown in section 3, and the real-case studies are presented in section 4. Section 5 provides further discussion of the results as well as a summary.

2. Numerical Method and Experiments

For this study, we used HWRFv3.7a (2015 operational model). This included the use of the upgraded model grid spacing for domains 1–3 of 18, 6, and 2 km, respectively, and 61 vertical model levels. Model physics packages for the operational HWRFv3.7a include the Ferrier-Aligo microphysics, Rapid Radiative Transfer Model for General Circulation Model longwave/shortwave radiation, simplified Arakawa-Schubert cumulus, modified Geophysical Fluid Dynamics Laboratory (GFDL) surface layer, and modified National Centers for Environmental Prediction Global Forecast System (GFS) planetary boundary layer schemes (Tallapragada et al., 2015). Three cases were used in this study: one using an idealized vortex and two real-case studies.

For the idealized TC, the initial vortex was generated using a maximum surface wind speed of 36 m s^{-1} at a radius of 45 km from the storm center. The vortex was embedded in a quiescent background whose temperature and humidity profiles were specified by the non-Saharan air layer sounding of Dunion and Marron (2008). Sea surface temperature (SST) was set to 29°C, and the idealized vortex was placed on an f-plane centered at 20°N. The complete details of the idealized setup are enumerated in Zhu and Zhu (2015). The simulation using this idealized vortex was run for nine days.

The real simulations were conducted for Hurricane Rita (2005) and Hurricane Edouard (2014). The cases were selected because they are classic examples of SEF and ERCs and have been the subject of several past research studies (e.g., Abarca et al., 2016; Abarca & Corbosiero, 2011; Bell et al., 2012; Didlake & Houze, 2011; Houze et al., 2007; Judt & Chen, 2010). Furthermore, both were well-sampled cases, and thus, the observations could be used to compare with the simulated ERCs. For the real case of Edouard (2014), initial and boundary conditions were supplied using six-hourly GFS data with 0.25° grid spacing. The simulations of Rita (2005) were forced using 1.0° grid resolution six-hourly GFS data. Due to the low resolution of the available GFS data, a bogus vortex generated by the GFDL model was blended with the GFS-driven initial conditions for the Rita simulations. Though the atmospheric model was not run coupled to the HWRF ocean model, daily real-time global SST data were used for creating the model boundary conditions in the real-case studies. Following the operational HWRF, the real-time
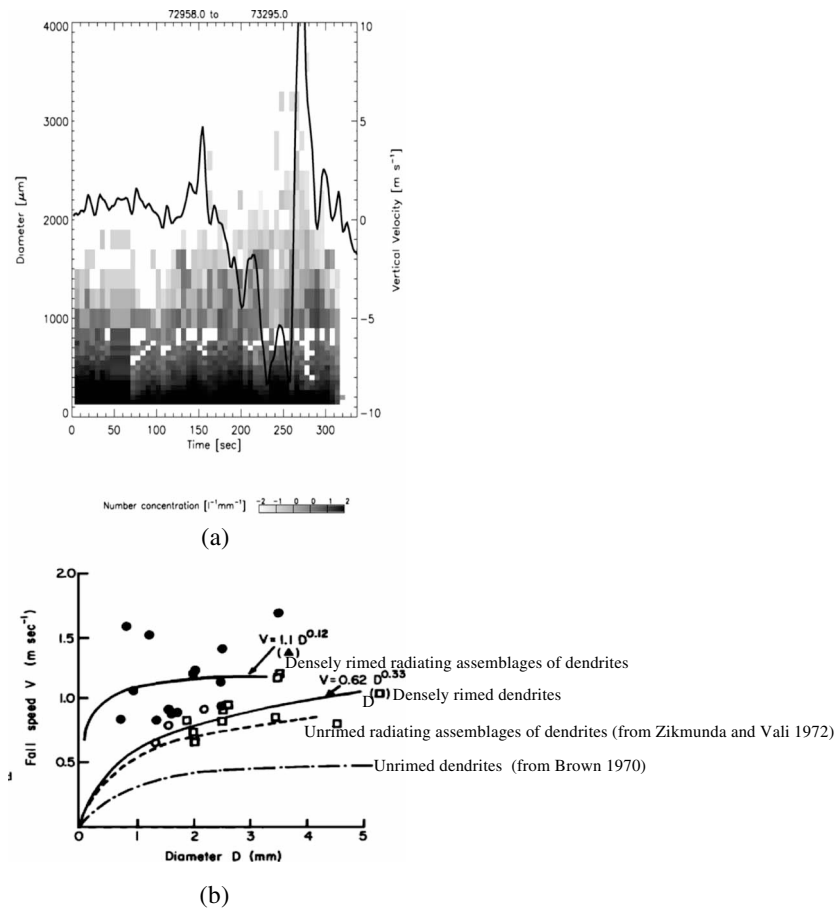
(a)

(b)

Figure 1. (a) Time series of number concentration (L^{-1} mm^{-1}) as a function of diameter (μm) from Hurricane Emily (1987) (from McFarquhar & Black, 2004) and (b) empirical relationship of snow fall speed (m s^{-1}) as a function of diameter for various classes of unrimed and rimed dendrites (from Locatelli & Hobbs, 1974).

simulations were run for a period of 126 h. The model runs for Rita (2005) and Edouard (2014) were initialized at 00 UTC 20 September 2005 and 00 UTC 14 September 2014, respectively.

In this study, our focus was on the impact of microphysics on SEF; in particular, the hydrometeor particle fall velocity was investigated. Zhu and Zhu (2015) showed that altering the snow terminal velocity can affect the occurrence and characteristics of SEF in WRF-ARW. However, the underlying mechanism of modulation of SEF by snow terminal velocity was not fully explored in their study. The investigation into particle fall velocity was also inspired by the observational study by McFarquhar and Black (2004), who examined the size distributions of snow and graupel particles near the melting layer using in situ microphysical data collected during Hurricane Norbert (1984) and Emily (1987). Figure 1a shows a time series of number concentration for various sizes of solid-phase hydrometeors for Hurricane Emily (1987) adopted from McFarquhar and Black (2004). It is clear that there were a large number of solid-phase particles with diameters smaller than 300 μm (0.3 mm). In another highly referenced study, Locatelli and Hobbs (1974) used observations to examine the fall speeds of various classes of solid-phase hydrometeors. Figure 1b shows the empirical relationship of particle fall speed as a function of particle size diameter adopted from Locatelli and Hobbs (1974). Based on the empirical relationship, the large number of particles with diameters smaller than 0.3 mm observed in McFarquhar and Black (2004) would correlate to fall speeds less than 0.2 m s^{-1}.

Given the expected commonality of fall speeds less than 0.2 m s^{-1} based on these observational studies, it is of interest to examine how well the simulated particle fall speeds by the operational HWRF match the observations. Figures 2a, 2c, and 2e show the distributions of hourly particle fall speed from the
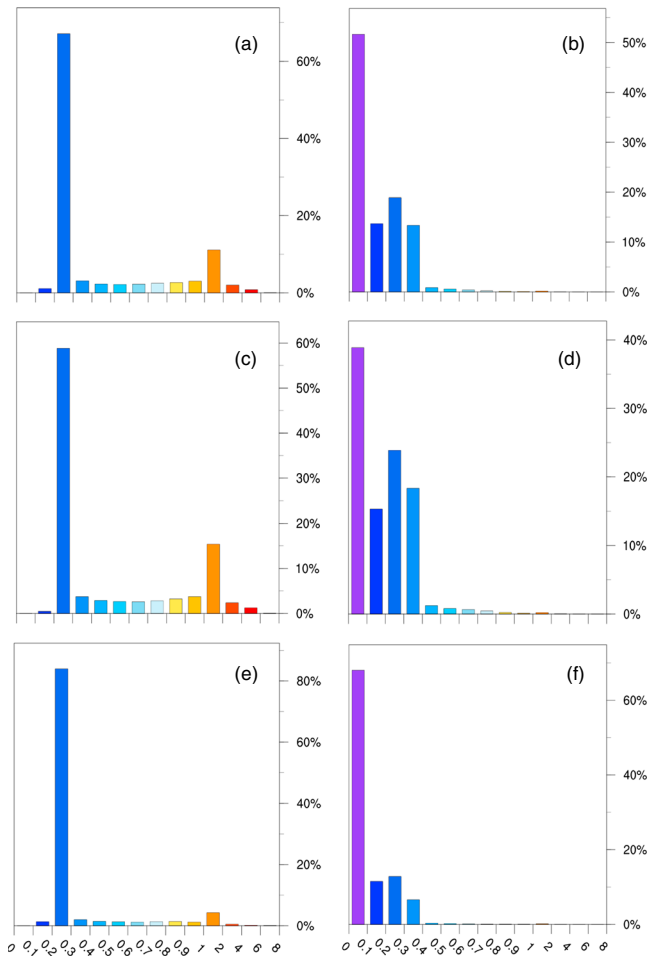
Figure 2. Histogram of hourly snow fall speed (m s^{-1}) for simulations using the (left) default Ferrier-Aligo microphysics scheme and (right) V_s * ¼ scheme. Data are plotted for the (a and b) idealized vortex, (c and d) Rita (2005), and (e and f) Edouard (2014) simulation.

three simulations using the HWRFv3.7a operational settings over the entire simulation period. In both idealized and real-case simulations, there is a large peak of particle fall speeds between 0.3 and 0.4 ms^{-1}, but there are very few solid-phase hydrometeors with fall speeds less than 0.2 m s^{-1}, a stark contrast to the particle fall speed distribution in real TCs according to the observations by McFarquhar and Black (2004). The result suggests that the operational HWRF is not producing the smallest, lightest solid-phase hydrometeors that are readily observed in real TCs. The question remains: are these smallest, lightest solid-phase hydrometeors important? If so, how do they affect the structure and evolution of a TC?

To address these questions, additional sensitivity experiments that can generate hydrometeor particles with fall speed less than 0.2 m s^{-1} are needed. Although it is not physically robust, the easiest way to do this is to artificially reduce the particle fall velocity. We emphasize that such a practice should not by any means be interpreted as tuning of microphysics. The only purpose of this reduction is to examine the importance of small and light hydrometeors to TCs structure, in particular, the importance to SEF. In the HWRFv3.7a operational Ferrier-Aligo microphysics scheme, snow, graupel, and ice are grouped together as one total solid-phase condensate. To account for these different classes of solid-phase hydrometeors, the mass-weighted fall speed of solid-phase condensate at each grid point in the model is calculated as follows,

$$V_s = V_{SI} \cdot \gamma_s \cdot [V_{rime}]^{3/2}, \tag{1}$$

Table 1
A List of All Experiments Presented

Experiment name	Initialization time	Description
Idealized1	00 UTC 1 January 1111	Operational settings
Idealized2	00 UTC 1 January 1111	$V_s \cdot \frac{1}{4}$
Rita1	00 UTC 20 September 2005	Operational settings
Rita2	00 UTC 20 September 2005	$V_s \cdot \frac{1}{4}$
Edouard1	00 UTC 14 September 2014	Operational Settings
Edouard2	00 UTC 14 September 2014	$V_s \cdot \frac{1}{4}$

where V_{SI} is the mass-weighted fall speed of unrimed ice, γ_s is an air resistance term, and V_{rime} is a term to account for particle fall speed increase due to riming and melting of the solid-phase condensate (Aligo et al., 2014). In the sensitivity experiments, everything is kept the same except that equation (1) was multiplied by an artificial factor (i.e., $V_s = V_s \cdot \alpha$). Different values of α were tested during the investigation. In this paper, only results from the control simulations and sensitivity experiments with $\alpha = \frac{1}{4}$ are presented. Table 1 lists the experiments presented in this study. Figures 2b, 2d, and 2f show the distributions of hourly particle fall speed from the three sensitivity experiments with $\alpha = \frac{1}{4}$ over the entire simulation period. With the reduced particle fall speed, the modified Ferrier-Aligo scheme produced a much greater fraction of hydrometeors with fall speeds less than 0.2 m s^{-1}. It is important to note that the simple reduction in particle fall velocity also eliminated some of the largest solid-phase hydrometeors that are likely present in real TCs. This is the drawback of the sensitivity experiments designed in this study. However, the analyses presented in the following sections show that these eliminated large particles do not appear to have much impact on SEF. The advantage of the sensitivity experiments is that they allow us to investigate how hydrometeors with fall speed less 0.2 m s^{-1}, which are absent in the HWRF operational simulations, affect SEF. Moreover, by the experiment design itself, such a change in microphysics is initiated in the upper levels rather than within the boundary layer. This will help identify if there is a different pathway other than bottom-up pathway to SEF. In the sections that follow, we will use the control and sensitivity experiments listed in Table 1 to illustrate that the change in radial transport and distribution of solid-phase hydrometeors resulting from the reduced particle fall velocity can lead to a top-down pathway to SEF.

3. Idealized Case

Figure 3 shows a Hovmöller diagram of azimuthally averaged 5 km vertical velocity and 1 km tangential velocity for Idealized1 (control simulation) and Idealized2 (experimental simulation). For Idealized1, a well-defined eyewall emerged approximately 15 h into the simulation, characterized by maximum vertical velocity of around 1.5 m s^{-1} at a radius of 20 km from the storm center. The eyewall gradually expanded radially outward, reaching a peak intensity at about 85 h into the simulation, with maximum vertical velocity of around 2.5 m s^{-1} and peak tangential wind speed of 70 m s^{-1}. There was some weaker, deep convection encompassing a large region outside of the eyewall associated with rainbands, but there was no well-defined moat region separating this outer convection from the eyewall, nor was there a secondary tangential wind maximum. The eyewall continued to expand radially outward in time. This eyewall expansion in HWRF idealized simulations was also demonstrated in Zhu et al. (2015). The storm began a period of weakening about 130 h into the simulation. This weakening continued throughout the rest of the simulation, with the eyewall becoming diffuse as it continued to propagate radially outward (Figure 3a).

The storm in Idealized2 evolved quite differently. In this model run, an intense eyewall developed at about 20 h into the simulation, slightly delayed compared to that in Idealized1. The eyewall moved radially outward for a brief period of several hours but then made a turn radially inward approximately 50 h into the simulation. At the same time, deep convection developed at a radius of 150 km from the TC center, with a well-defined downdraft moat region separating these two features. Over the next 30 h, the outer rainband convection continued to strengthen, move radially inward, and eventually evolved into the secondary eyewall. The secondary eyewall remained cleanly separated from the primary eyewall by the well-defined downdraft moat region. As the secondary eyewall strengthened, the primary eyewall weakened. By about 75 h into the simulation, the inner eyewall convection and the associated tangential wind maximum were no longer visible, a new tangential wind maximum was present at a radius of 40 km from the storm center, and the ERC completed. The stages of SEF and ERC completion are indicated in the figure. The newly formed eyewall then continued to intensify and gradually move radially outward for the remainder of the simulation (Figure 3b).

Compared to the clean concentric double eyewalls separated by a well-defined moat downdraft region shown in Idealized2, there was a weak and diffuse SEF-like event occurring around 40–60 h into the
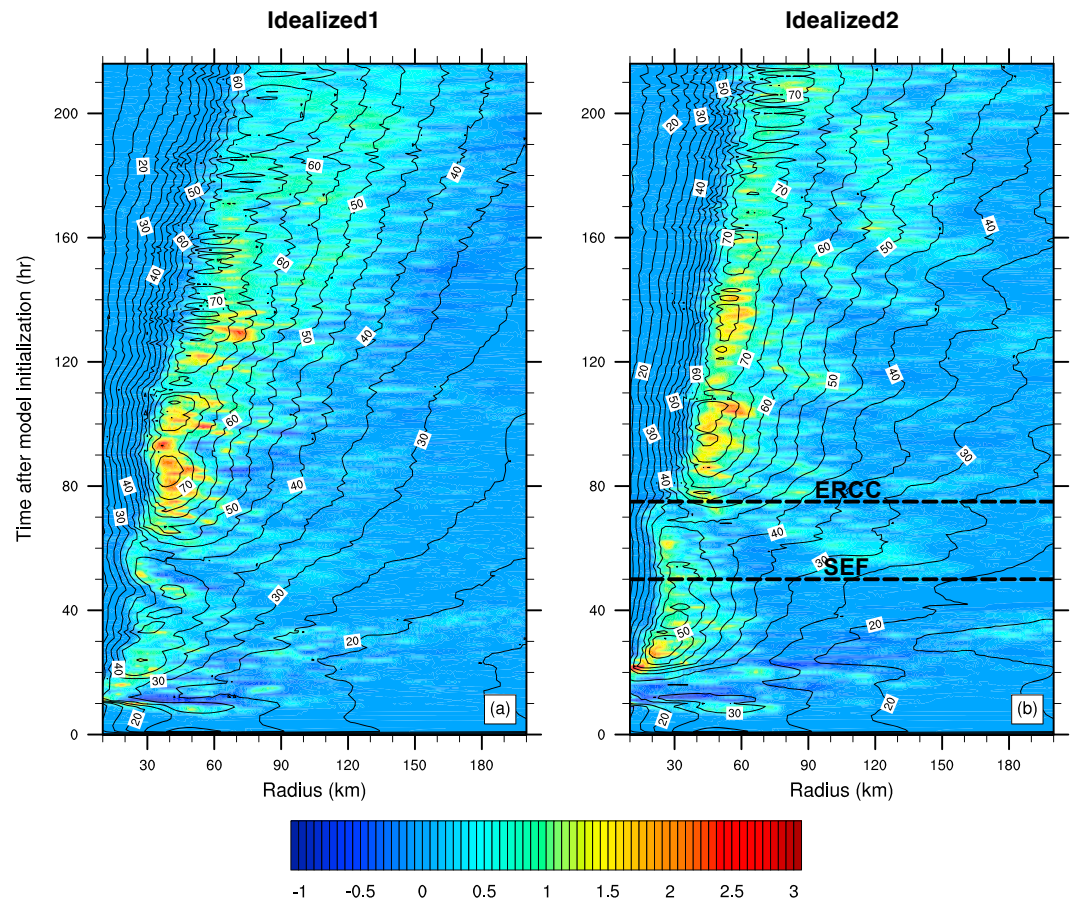
Figure 3. (a) Azimuthally averaged 5 km vertical velocity (shading, m s^{-1}) and 1 km tangential velocity (contours, m s^{-1}) for (a) Idealized1 and (b) Idealized2. Times of SEF and ERC completion (ERCC) are notated for Idealized2.

simulation in Idealized1. It should be noted that such SEF-like features are frequently observed in HWRF simulations, and they do not pertain only to HWRF. Weak SEF-like features have also been demonstrated in WRF-ARW simulations (Zhu & Zhu, 2015), where they were termed "aborted ERCs." Often, these SEF-like features do not possess the characteristics of SEF observed in real TCs. They either merge with the inner eyewall or dissipate to result in a long-lived inner eyewall. This does not appear to be trivial both scientifically and operationally, as the occurrence of these features prohibits HWRF's ability to simulate SEF with observed characteristics.

To further highlight the differences between the SEF-like feature in Idealized1 and the SEF event in Idealized2, Figure 4 shows the radius-height structure of azimuthal-mean vertical velocity, total condensate, convergence of radial flow, and transverse circulation averaged over 45–55 h in Idealized1 compared with that averaged over 54–66 h in Idealized2. There was a well-defined primary eyewall in both simulations, although the vertical velocity suggests that the primary eyewall was much stronger in Idealized2. The characteristics and relative strengths of the transverse circulation were qualitatively similar for the simulations, with strong near-surface radial inflow becoming lifted aloft within the primary eyewall and eventually radially outward in the upper troposphere. There was a strong secondary vertical velocity maximum in Idealized2, tilting radially outward from a radius of approximately 70 km in the boundary layer to a radius of 140 km in the upper troposphere. This secondary maximum of vertical velocity, a signature of a secondary eyewall, was cleanly separated from the primary eyewall by a well-defined downdraft moat region located 40–70 km from the storm center. This radial-height structure of vertical velocity is consistent with the observed structure of double eyewalls in real TCs (e.g., Didlake & Houze, 2011). In addition to this secondary vertical velocity maximum, there was a notable secondary maximum of radial convergence within the SEF region for Idealized2.
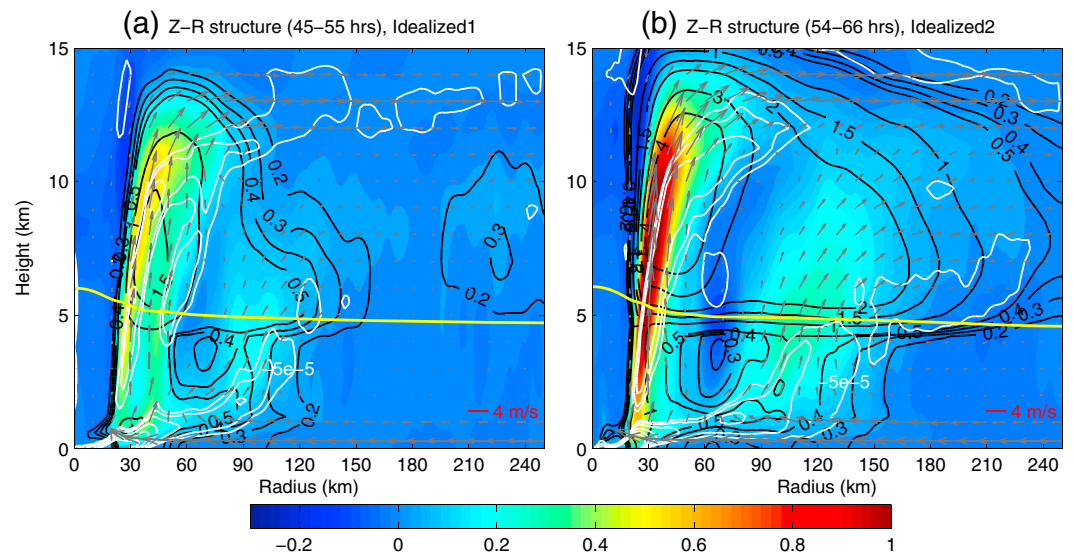
Figure 4. Radius-height cross section of azimuthally averaged vertical velocity (shading, m s^{-1}), total condensate (black contours, g kg^{-1}), radial convergence (white contours, s^{-1}), and transverse circulation (vectors, m s^{-1}) for (a) Idealized1 and (b) Idealized2. The yellow line denotes the freezing level. Hourly data are temporally averaged from 45 to 55 h and 54 to 66 h for Idealized1 and Idealized2 respectfully.

We wish to emphasize that the peak of this secondary radial convergence was located above the boundary layer in the outer rainband region. The evolution of radius-height structure of the secondary maximum of radial flow convergence, which reflects the dynamic response to diabatic heating of outer rainband convection in triggering SEF, will be discussed in detail shortly. In Idealized1, although similar in appearance of the radius-height structure at the first glance, there are notable differences of the double eyewall structure between the two simulations. The secondary vertical velocity maximum and moat downdrafts in Idealized1 were much weaker than those of Idealized2 and observed characteristics of concentric eyewalls in real TCs. Furthermore, the radial distance between the primary and secondary vertical velocity maxima and the radial extent of the convergence in Idealized1 are much smaller than in Idealized2. To understand the underlying reason why HWRF and other models tend to produce the SEF-like features without possessing the observed characteristics of SEF is one of the motivations for this study. Using real-case simulation of Edouard (2014), we shall show later that the SEF-like features in the control simulations are triggered by different physical processes from those of SEF events in the sensitivity experiments with reduced particle fall velocity.

One of the key differences between the two simulations is the amount and radial-height distribution of total condensate. A much larger total condensate in the primary eyewall was generated in Idealized2 than in Idealized1. Furthermore, the total condensate above the freezing level was advected to farther radii from the storm center in Idealized2. This result is somewhat expected since smaller particle fall velocities increase the airborne time of lofted hydrometeors, and thus, reduce condensate fallout in the primary eyewall region, allowing the transverse circulation to transport the hydrometeor particles to outer radii. Evidence of enhanced radial transport of lofted hydrometeors due to the reduction of particle fall velocity from a budget analysis of total condensate will be provided and further discussed later in the real-case simulations of Edouard (2014). While the cause for the differences in the radial-height structure of hydrometeors may be clear, what remains less transparent is the implication of the radial transport and distribution of hydrometeors to triggering SEF.

To better understand the mechanism that triggers SEF in the sensitivity experiment, we traced and scrutinized the evolution of several dynamic and thermodynamic fields in the TC inner-core region during the course of SEF in Idealized2. As a summary, Figure 5 shows the azimuthally averaged vertical velocity, total condensate, convergence of radial flow, tangential wind speed, and transverse circulation at several key stages during the lifecycle of SEF of Idealized2. At the 30th hour into the simulation, a well-defined
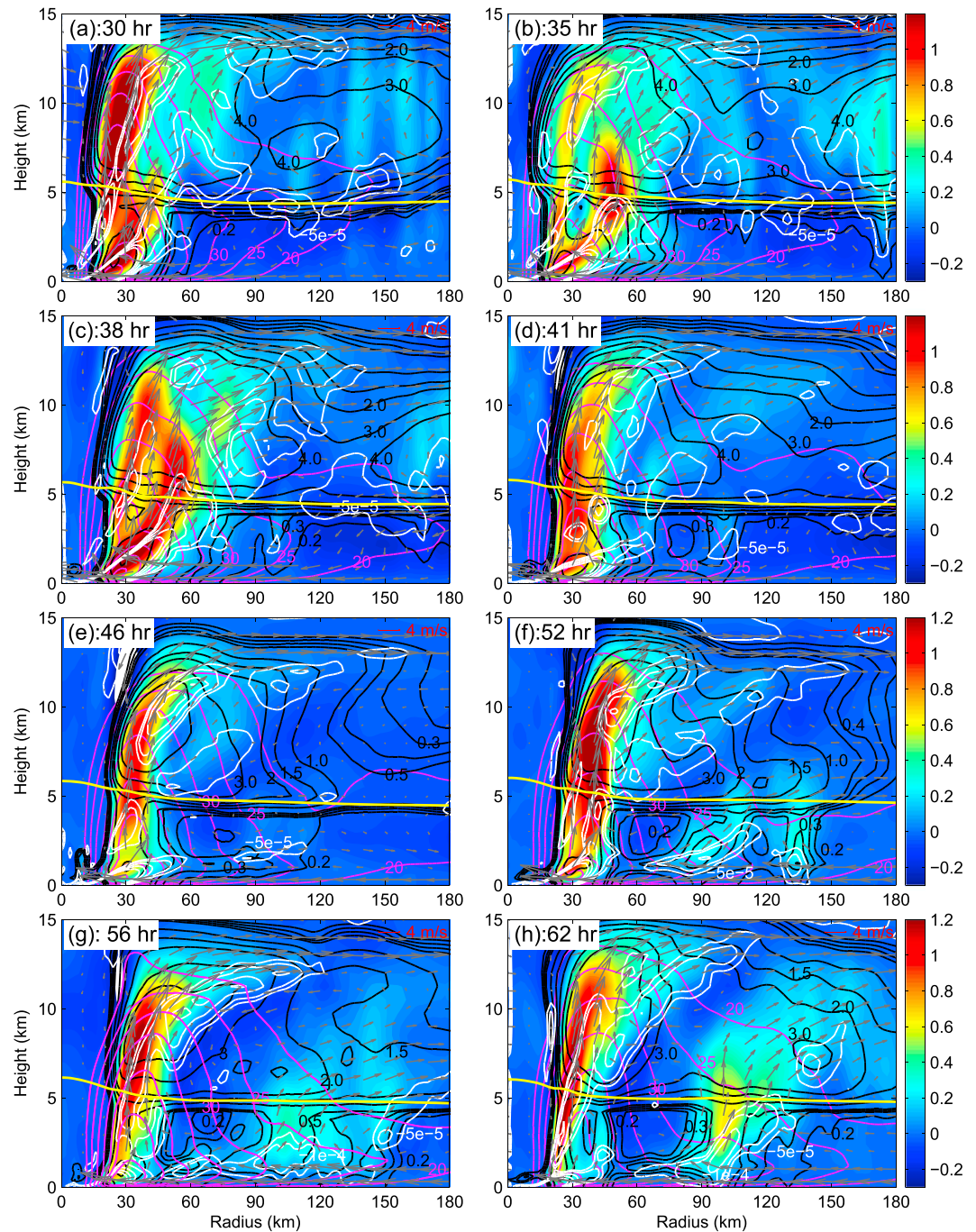
Figure 5. Radius-height cross section of azimuthally averaged vertical velocity (shading, m s^{-1}), total condensate (black contours, g kg^{-1}), radial convergence (white contours, s^{-1}), tangential winds (purple contours, m s^{-1}), and transverse circulation (vectors, m s^{-1}) at different stages for Idealized2. The yellow line denotes the freezing level.

primary eyewall characterized by a strong updraft was located approximately 20 km from the storm center (Figure 5a). At outer radii, updrafts associated with sporadic deep convection are evident mainly above the freezing line. Because the updrafts below 5 km were fairly weak, the outer rainband convection was likely fostered by the in-cloud latent heating in the upper atmosphere rather than boundary layer processes at this stage. A large amount of solid-phase hydrometeors are visible in this outer rainband region above the freezing level. The rainband convection induces midlevel convergence (white contours), evident just below the corresponding updrafts at this time, which is consistent with the Sawyer-Eliassen diagnoses performed
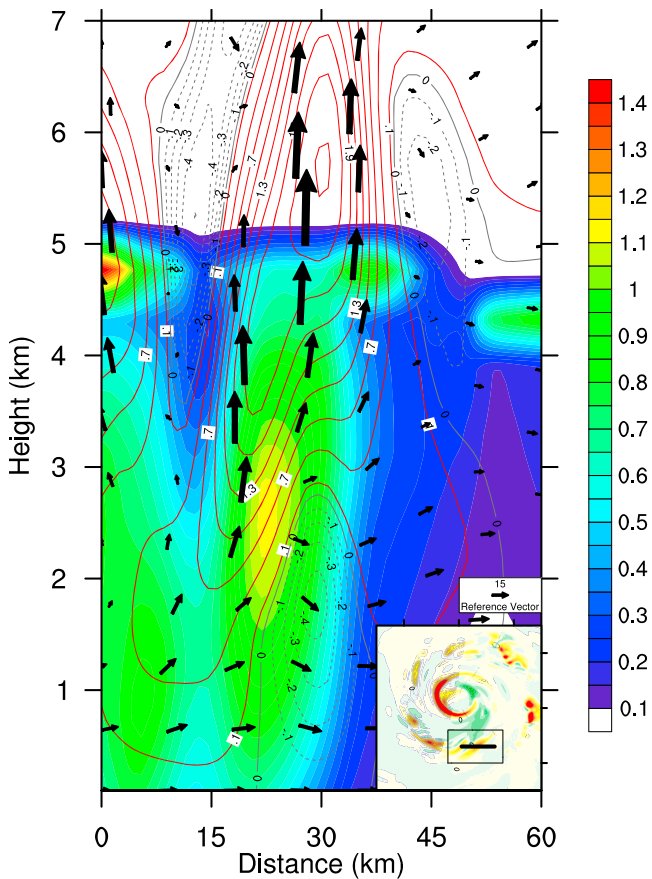
Figure 6. Radius-height cross section of rain water mixing ratio (shading, g kg^{-1}), vertical velocity (m s^{-1}), and wind speed (vectors, m s^{-1}). The vertical velocity component of the vectors has been scaled by a factor of 30. The cross-section is taken 53 h into the Idealized2 simulation from the convective region indicated in the inset figure. Vertical velocity at a height of 5 km (shading, m s^{-1}) is plotted in the inset figure.

by Zhu and Zhu (2014) (Figures 13c and 13f in their paper). Over the next 8 h, condensate located approximately 110 km from the storm center began extending downward below the freezing level, indicating the formation of a steady precipitation in the region (Figures 5b and 5c). By the 41st hour into the simulation, cloud and rainwater encompass the lower troposphere at this radius (Figure 5d). The precipitation and associated evaporative cooling result in penetrative downdrafts, which in turn promote the development of low-level convection, as indicated by the appearance of low-level convective updrafts in the outer rainband region. Evidence for promotion of low-level convection by the penetrative downdraft resulting from precipitation is provided in Figure 6, which shows the vertical structure of an arbitrary outer rainband convective episode. It is clear from the figure that the precipitation induces a downdraft (dashed black contours) below the rainwater mixing ratio maximum (shaded). The lifting created by the penetrative downdraft invigorates the convective updraft (solid red contours).

At the 46th hour into the simulation, a radial flow convergence maximum resulting from the development of the low-level convection is evident at a height just above the boundary layer, defined by the inflow layer (Figure 5e). As a dynamic response, near-surface tangential wind below the rainband low-level convection expanded, consistent with the Sawyer-Eliassen analyses (not shown). Although they remained weak, the radial flow convergence near the top of the boundary layer and the expansion of the near-surface winds served to link the initially loosely connected boundary layer processes and midlevel convection. Once the channel was established, it kicked off a positive feedback among low-level convection, convergence of radial flow in the upper boundary layer, acceleration of surface tangential winds, and surface evaporation that ultimately led to the continued rapid development of outer rainband convection and the subsequent formation of the secondary eyewall. The positive feedback cycle is clearly reflected in the change of the radius-height structure over the next 10 h in the simulation, as different processes worked in concert to result in well-defined double eyewalls cleanly separated by a distinct moat downdraft (Figures 5f–5h).

It should be pointed out that the second part of the SEF depicted in Figure 5 was similar to the SEF pathway described in Huang et al. (2012), who also emphasized the role of boundary layer radial flow convergence and near-surface tangential wind expansion in SEF. However, it is apparent that in Idealized2, the triggering of SEF was not initiated from the boundary layer but rather from the hydrometeor fallout in the outer rainband region. The penetrative downdraft resulting from evaporative cooling of precipitation lifted the sporadic updraft in the area, leading to the enhancement of local convection, which in turn induced the radial flow convergence below the convection. As the radial flow convergence moved down into the boundary layer, it caused the eruption of high entropy air out of the boundary layer, fostering further convection in the SEF region in a positive feedback process.

In the pathway to SEF described above, a key feature that determines the secondary precipitation region is the radial-height distribution of solid-phase hydrometeors. In Idealized2, the reduced particle fall velocities allowed solid-phase hydrometeors to be transported to farther radii from the primary eyewall by the upper tropospheric radial outflow, where the emergence of a steady secondary precipitation region promoted the development of rainband convection. Here the large radial distance between the outer rainband convection and primary eyewall appeared to be critical to SEF, since it permitted the development of a moat separating the outer rainband convection from the primary eyewall, so that the former could evolve with minimal interference from the latter. In contrast, the large particle fall velocities in Idealized1 limited the radial transport of solid-phase hydrometeors (Figure 4a). As a result, the secondary precipitation region emerged at radii much

closer to the primary eyewall than those in Idealized2 (not shown here). Although the precipitation did induce rainband convection in the same way as that in Idealized2, the convection was too close to the primary eyewall, leaving insufficient radial space for a full development of a moat. Without the moat, the rainband convection for Idealized1 was able to move radially inward with little resistance and merge with the eyewall deep convection, resulting in a long-lived inner eyewall.

We want to acknowledge that by the nature of the experimental design, one might get an impression that we are suggesting that SEF is directly modulated by particle fall velocity. While the evidence provided here reveals a top-down pathway to SEF, we do not suggest that SEF can be solely driven by microphysical processes aloft alone without interaction with the boundary layer processes. In the sensitivity experiment, a direct effect of reducing particle fall velocity is to lengthen the airborne time of hydrometeors generated in the eyewall so that the lofted hydrometeors tend to be transported farther radially outward by the outflow. This enhanced radial transport of lofted hydrometeors leads to a chain of events. A critical event here is the precipitation resulting from the fallout of hydrometeors at their stagnation radii, which serves as a mechanism to bridge the microphysical and boundary layer processes. It is the downdraft induced by the evaporative cooling of precipitation that promotes local rainband convection. In Figure 5, there are several peaks of condensate in the outer radii. These peaks of condensate are apparently not directly linked to the upper level outflow; rather, they are associated with local convective episodes that were initiated and enhanced by the penetrative downdrafts resulting from precipitation. Therefore, these peaks of condensate may be considered to be indirectly influenced by the change in particle fall velocity via the interaction between the microphysical and boundary layer processes. Reduction in particle fall velocity results in larger stagnation radii of transported hydrometeors, which causes the rainband convection to occur at farther radii. The wider radial distance between the inner eyewall and outer rainband convection allows for the full development of a moat region, permitting outer rainband convection to develop freely from the inner eyewall and evolve into a secondary eyewall. With the larger particle fall velocities in the control experiments, the fundamental process involving the interaction between microphysical and boundary layer processes remains the same. However, the rapid fallout of hydrometeors causes the outer rainband convection to develop at radii closer to the inner eyewall, leaving insufficient radial space to develop a well-defined moat region. Without a persistent moat downdraft, the outer rainband convection may either move inward and merge with the inner eyewall or result in a SEF-like structure with a much narrower radial width between the inner and outer eyewalls than that of observed SEF in real TCs.

One question remaining is whether the control of SEF by the distribution of solid-phase hydrometeors pertains only to the idealized TC vortex constructed in this study or is valid for real TCs. To address this issue, we performed real-case simulations with the same experimental design as the idealized simulations.

4. Real Cases

In this section, we present results from real simulations of Hurricanes Rita (2005) and Edouard (2014).

4.1. Rita (2005)

Figure 7 shows the time series of the azimuthally averaged 5 km vertical velocity and 1 km tangential velocity for the two Rita (2005) simulations. In Rita1, an intense eyewall emerged at about 12 UTC on 21 September. The eyewall remained at a relatively constant radius of 25–30 km from the storm center for the first two days, before moving slightly radially outward to a radius of 45 km on 23 September. There is evidence of sporadic deep convection outside the eyewall, but this convection quickly merged with the eyewall. While there is some indication of a radial expansion in the tangential winds that is typical of SEF, there was no clear secondary maximum in these tangential winds throughout the simulation. Early on 24 September, the eyewall weakened as the storm made landfall (Figure 7a).

The time series of azimuthally averaged 5 km vertical velocity and 1 km tangential velocity for Rita2 is in stark contrast to Rita1. The primary eyewall was much weaker than that associated with Rita1. The primary eyewall reached peak intensity at around 06 UTC 22 September. At this time, a secondary maximum in vertical velocity associated with the outer rainband convection developed at a radius of 120 km from the storm center. This outer rainband convection propagated inward and eventually developed into the secondary eyewall. The tangential winds began expanding radially outward at this time, with a clear secondary maximum in
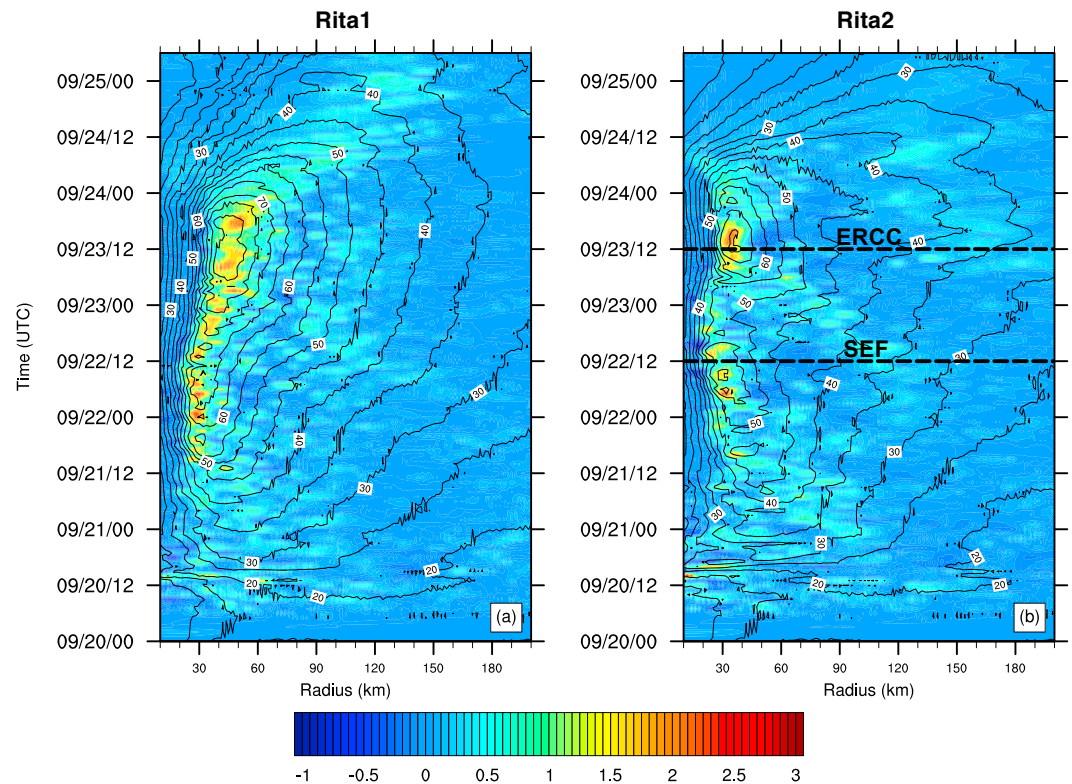
Figure 7. Time series of azimuthally averaged 5 km vertical velocity (shading, m s^{-1}) and 1 km tangential velocity (contours, m s^{-1}) for (a) Rita1 and (b) Rita2. Times of SEF and ERCC are notated for Rita2.

tangential winds visible early on 23 September. As the primary eyewall weakened, the secondary eyewall moved radially inward, reaching a final radius of around 30 km from the storm center at 12 UTC 23 September (Figure 7b). The timing of the simulated SEF and ERC, approximately from 12 UTC 22 September to 12 UTC 23 September, is consistent with observations (e.g., Bell et al., 2012; Didlake & Houze, 2011; Houze et al., 2007), although the detailed simulation-observation comparison of vortex structure suggests that the simulated SEF in Rita2 was delayed by a few hours (presented later).

Radar reflectivity from Electra Doppler Radar (ELDORA) at 18 UTC 22 September along with the simulated radar reflectivity for Rita1 and Rita2 at 21 UTC 22 September is plotted in Figure 8. There was a clear maximum in observed radar reflectivity associated with the primary eyewall near the center of the storm. Adjacent to this primary eyewall, there was a distinct moat region void of convection, particularly in the northern quadrants of the TC. At a normalized distance of $r/rmax = 1.75$ from the storm center, there was a distinct, nearly symmetrical ring of convection associated with the secondary eyewall (Figure 8a). Rita1 generated a TC vortex with a much larger eyewall surrounded by a broad region of deep convection compared to the ELDORA radar data (Figure 8b). The overall TC structure in Rita2 was much more aligned with the observations. There was an area of high reflectivity near the storm center associated with the primary eyewall, with similar reflectivity values to the observed. The size of the eye and the width of the inner eyewall in Rita2 also closely matched to the radar data. The simulated reflectivities of both inner and outer eyewalls were comparable to the observed radar reflectivity, although the simulated concentric eyewalls appeared about 3 h later. There was a clear moat region void of convection in between the inner and outer eyewalls, particularly to the north of the TC primary eyewall, also consistent with radar observations (Figure 8c).

The azimuthally and temporally averaged vortex radial-height structure for both simulations during the time of SEF in Rita2 is shown in Figure 9. Unlike the idealized simulations, the primary eyewall was stronger in the control simulation than in the experiment with reduced fall speed, demonstrated by the larger vertical velocities. The transverse circulation was similar for Rita1 and Rita2, although the condensate above the freezing level extended to farther radii in Rita2 than in Rita1, a feature that reflects the reduction of particle fall speed
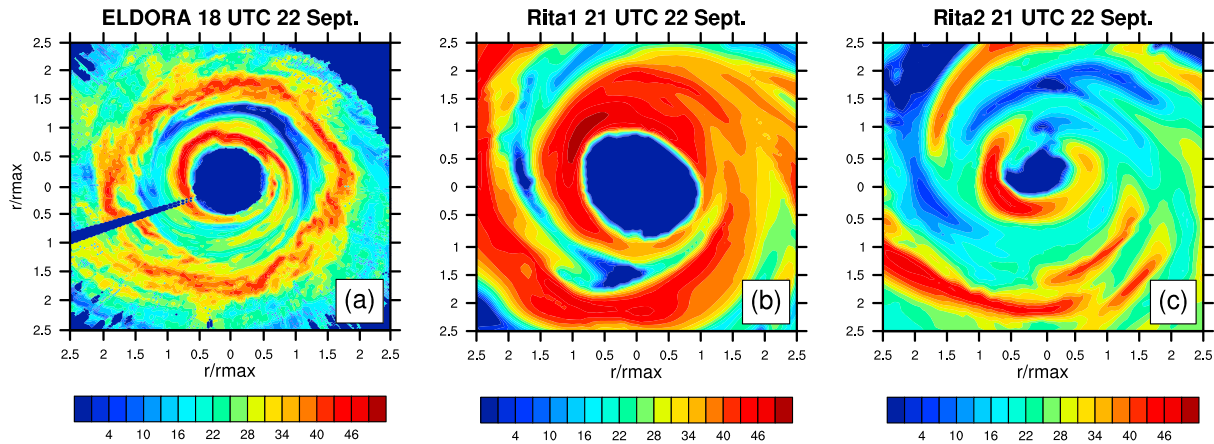
Figure 8. 4 km radar reflectivity (dBZ) at (a) 18 UTC 22 September from ELDORA radar, as in *Didlake and Houze* (2011), (b) 21 UTC 22 September for Rita1, and (c) 21 UTC 22 September for Rita2.

in Rita2 and is consistent with the results from the idealized simulations. In Rita2, there was a secondary maximum of vertical velocity centered at the radius of 100 km, which was cleanly separated from the inner eyewall by a moat region void of convection over a large radial distance extending 50–100 km from the storm center in the lower troposphere. Outer rainband convection was also evident in Rita1, but it was only marginally separated from the primary eyewall by a very weak and narrow moat in the lower troposphere. As discussed earlier for the idealized simulations, such outer rainband convection can easily move inward and merge with the primary eyewall to result in a long-lived eyewall without eyewall replacement. Indeed, the eyewall and rainband convection in the midtroposphere to upper troposphere were connected in Rita1. As in Idealized2, there is evidence of a clear secondary radial flow convergence maximum above the boundary layer in Rita2 approximately 120 km from the storm center.

The azimuthal-mean, radial-height structures of the vortex at key stages during the SEF and ERC in Rita2 are shown in Figure 10. The SEF in this case evolved in a similar fashion to Idealized2, namely, convective processes above the boundary layer triggered SEF. At 16 UTC 21 September, hydrometeor fallout began at a
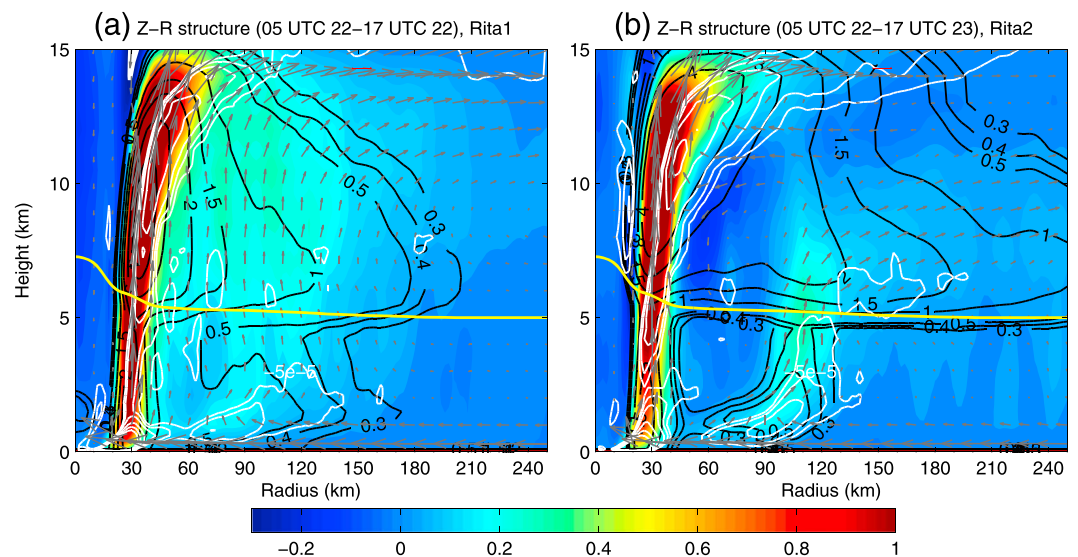

Figure 9. Radius-height cross section of azimuthally averaged vertical velocity (shading, m s^{-1}), total condensate (black contours, g kg^{-1}), radial convergence (white contours, s^{-1}), and transverse circulation (vectors, m s^{-1}) for (a) Rita1 and (b) Rita2. The yellow line denotes the freezing level. Hourly data are temporally averaged from 05 UTC 22 September to 17 UTC 22 September, a key period for SEF in Rita2.
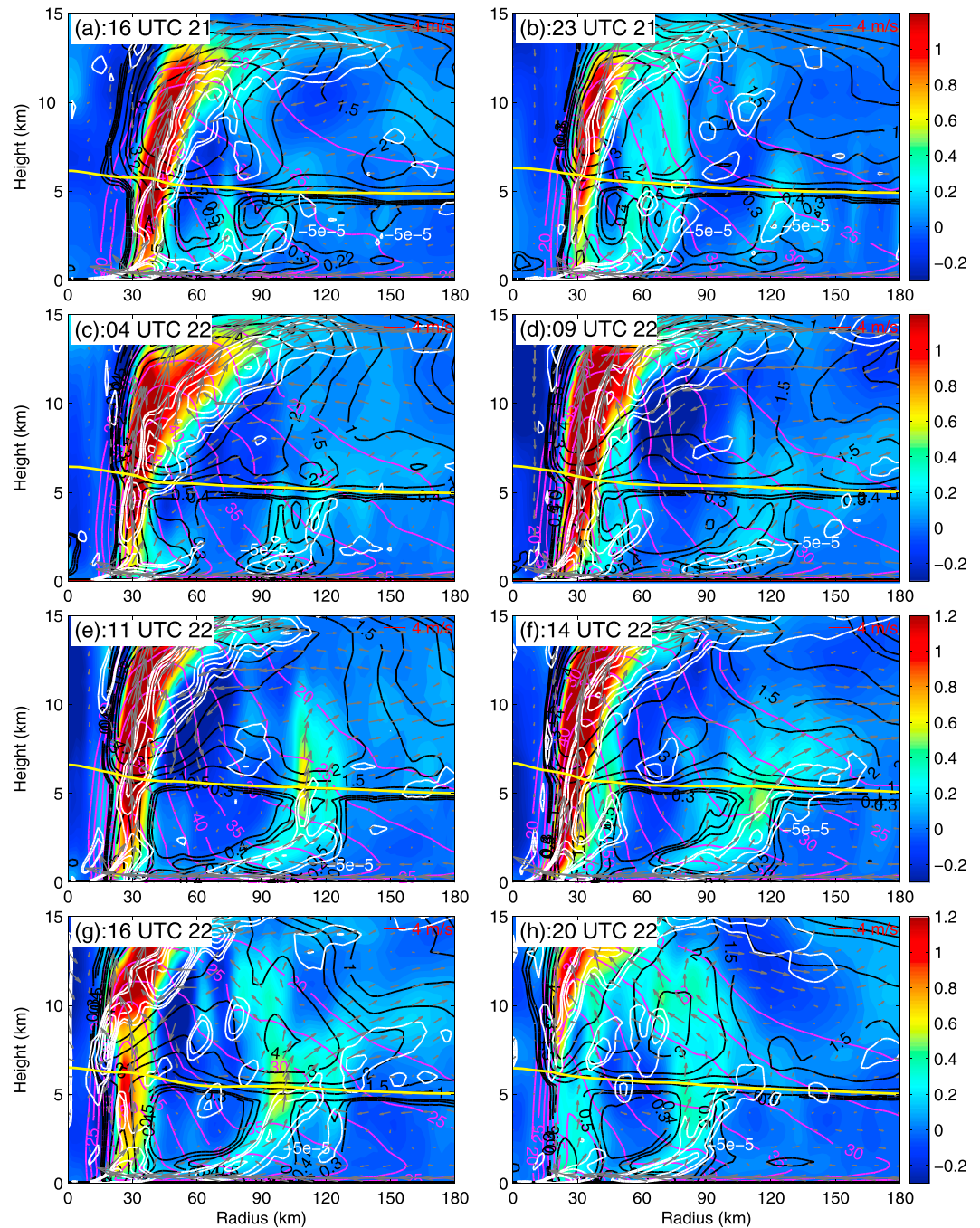
Figure 10. Radius-height cross section of azimuthally averaged vertical velocity (shading, m s^{-1}), total condensate (black contours, g kg^{-1}), radial convergence (white contours, s^{-1}), and tangential winds (purple contours, m s^{-1}), and transverse circulation (vectors, m s^{-1}) at different stages of SEF for Rita2. The yellow line denotes the freezing level.

radius approximately 150 km from the storm center (Figure 10a). It gradually extended downward and resulted in a steady precipitation region over the next 7 h. Evaporative cooling resulted in the development of a penetrative downdraft in this region. This downdraft played a critical role in lifting the low-level weak updraft to promote the development of local convection, which in turn induced convergence of radial flow below the convection (Figure 10b). As the convergence extended down into the boundary layer, it triggered the eruption of high entropy air out of the boundary layer and kicked off the positive feedback between convection and boundary layer processes, leading to the rapid development of outer rainband convection
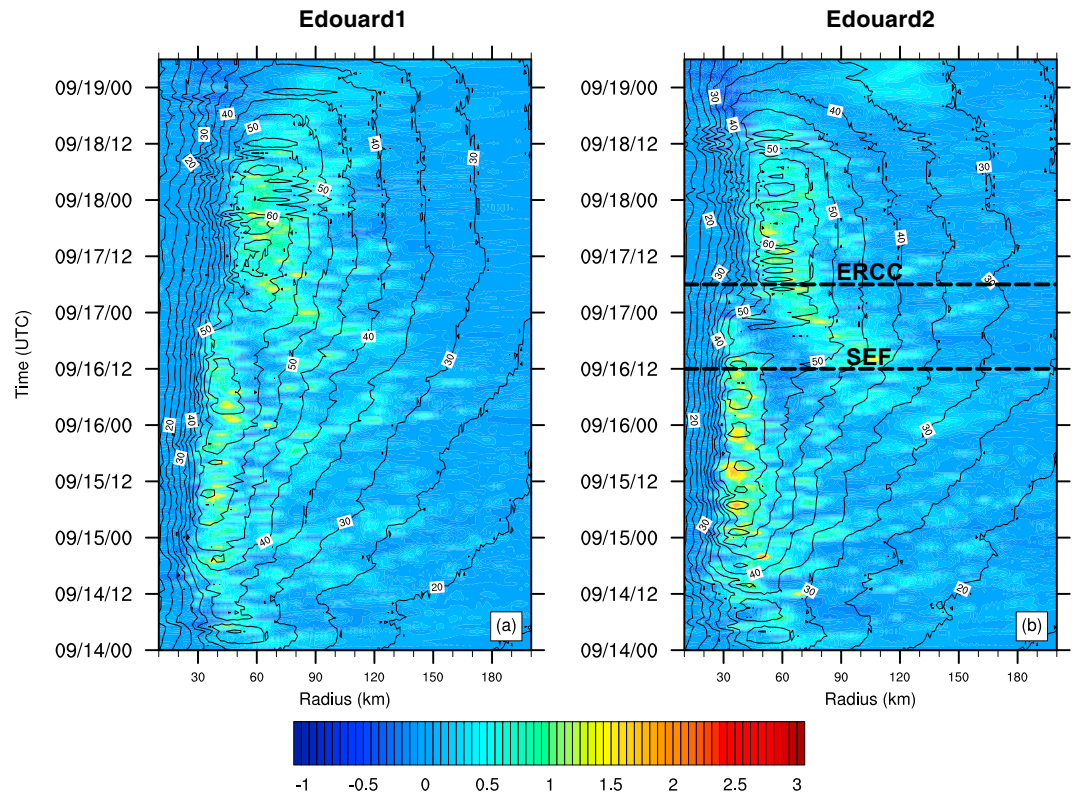
Figure 11. Time series of azimuthally averaged 5 km vertical velocity (shading, m s^{-1}) and 1 km tangential velocity (contours, m s^{-1}) for (a) Edouard1 and (b) Edouard2. Times of SEF and ERCC are notated for Edouard2.

(Figures 10c–10e). As in the idealized case, the large radial distance between the outer rainband convection and eyewall deep convection appear to be a key here. It allowed for the full development of a moat downdraft, which prevented the rainband from moving inward and merging with the inner eyewall. As such, the rainband convection was able to develop freely, which eventually evolved into a secondary eyewall associated with a well-defined secondary maximum of tangential winds (Figures 10f and 10g). At 20 UTC 22 September, the primary eyewall weakened, indicating the conclusion of the ERC event (Figure 10h). Soon thereafter, the inner eyewall dissipated and the newly developed outer eyewall took the role of the primary eyewall for the vortex.

4.2. Edouard (2014)

The time series of azimuthally averaged 5 km vertical velocity and 1 km tangential velocity for the Edouard (2014) simulations are plotted in Figure 11. In Edouard1 (control simulation), an eyewall developed early in the simulation at a radius of 60 km from the storm center. The convection associated with the eyewall gradually intensified and moved radially inward to a radius of 30 km. Sporadic convection developed beginning at 00 UTC 15 September at various radii outside of the eyewall. There is some indication of SEF from 18 UTC 16 September to 09 UTC 17 September, but it was not clearly separated from the primary eyewall. A detailed analysis of this event will be discussed shortly. The eyewall gradually moved radially outward over the next several days, before the storm weakened after 12 UTC 18 September (Figure 11a). Edouard2 (experimental simulation) underwent a similar evolution through 12 UTC 16 September. At this time, however, a concentrated area of convection developed at a radius of 120 km from the storm center. An outward extension of the tangential winds was also evident. Over the next 12 h, the outer rainband convection intensified, moved radially inward, and developed into the secondary eyewall, which eventually reached a radius of 60 km at 06 UTC 17 September. In the meantime, the primary eyewall weakened, moved slightly radially inward, and eventually dissipated at 00 UTC 17 September. The well-defined double eyewall structure cleanly separated by a moat downdraft is visible from 12 UTC 16 September to 00 UTC 17 September (Figure 11b).
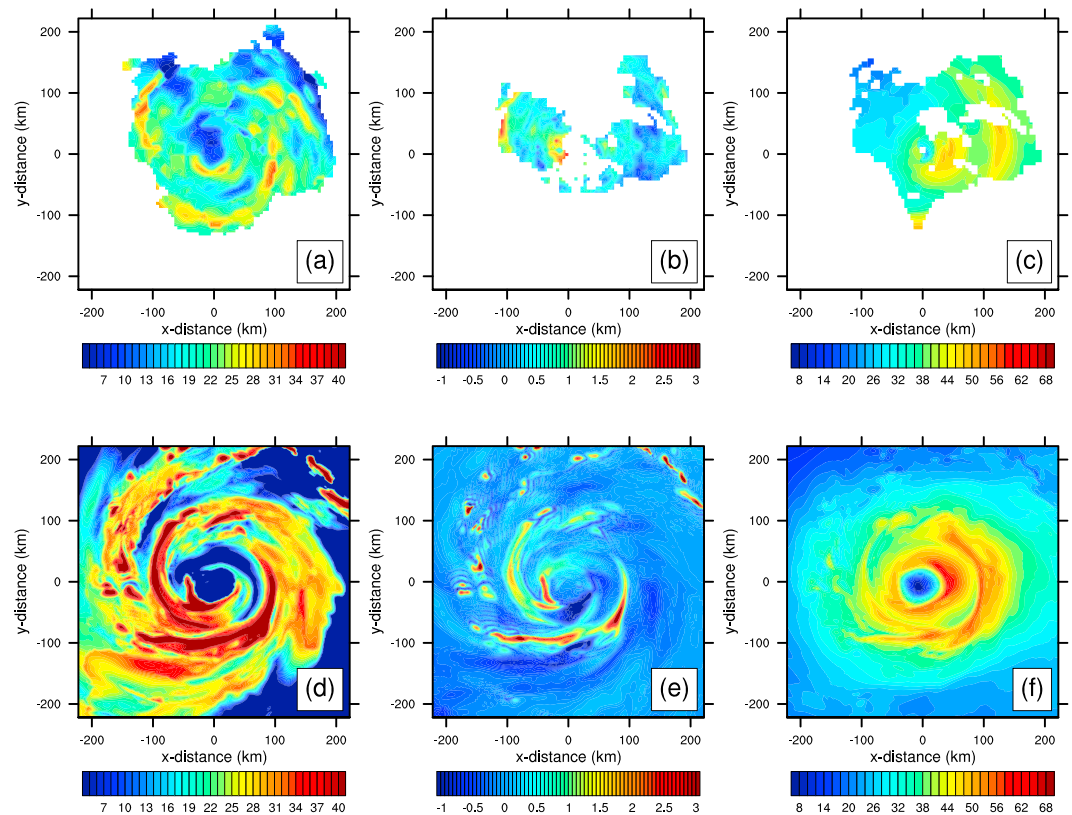
Figure 12. (a–c) 3 km radar reflectivity (dBZ), vertical velocity (m s^{-1}), and wind speed (m s^{-1}) from NOAA N42 aircraft observations centered at 1720 UTC 16 September; (d–f) same as Figures 12a–12c but for Edouard2 at 17 UTC 16 September.

We showed previously that the simulated timing and radial location of SEF in Rita2 was qualitatively consistent with observations. To verify the SEF in Edouard2, data from a 6 hour NOAA N42 flight centered at 1720 UTC 16 September were acquired and is plotted along with the model output of Edouard2 at 17 UTC 16 September in Figure 12. There were two distinct maxima of observed radar reflectivity and vertical velocity associated with the primary and secondary eyewalls visible in the observations, with the secondary eyewall located approximately 100 km from the TC center. Between the two regions of deep convection, there was a distinct moat region of much weaker convection, with low reflectivity values and negative vertical velocities associated with downdrafts (Figures 12a and 12b). There was also evidence of an observed secondary wind maximum, consistent with the presence SEF (Figure 12c).

The vortex inner-core features of Edouard2 closely matched the observations described above. There was a clear maximum in simulated radar reflectivity and vertical velocity associated with the primary eyewall in the western quadrants of the TC at this time. There was a secondary maximum in convection associated with the secondary eyewall located at a similar radial location to what was observed. In between these two regions, there was a distinct moat region of weak convection (Figures 12d and 12e). There were two distinct maxima in wind speeds at this time, indicative of a concentric double eyewall structure. The simulated asymmetric wind field, with larger wind speed on the eastern hemisphere of the TC, was also remarkably similar to observations (Figure 12f).

The vertical structure of the concentric double eyewalls in Edouard2 was also qualitatively consistent with observations. Figure 13 shows the azimuthal-mean radius-height structure of the observed radar reflectivity and wind speed at 1720 UTC 16 September compared with those from Edouard2 at 17 UTC 16 September. Edouard2 somewhat overestimated the storm intensity, as indicated by the larger magnitudes of simulated reflectivity and wind speeds compared to what were observed. We note, however, that the azimuthally averaged observed fields are likely skewed because of the lack of data at several azimuthals (Nolan et al., 2014). Furthermore, the simple algorithm used to calculate radar reflectivity from the simulated hydrometeor
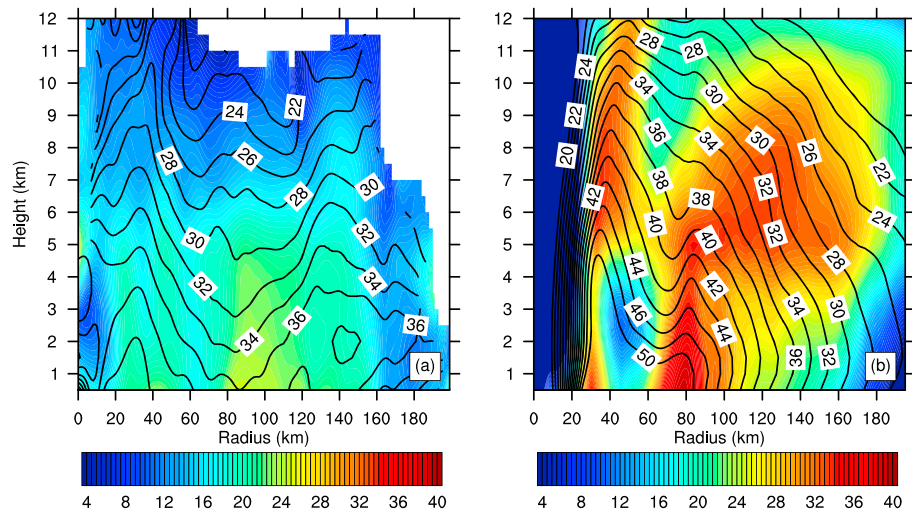
Figure 13. Azimuthally averaged radar reflectivity (dBZ, shading) and wind speed (m s^{-1}, contours) (a) observed at 1720 UTC 16 September and (b) for Edouard2 at 17 UTC 16 September.

mixing ratio may lead to an overestimation. Nonetheless, the overall vertical structures of the radar reflectivity and wind speed fields were similar between Edouard2 and observations. There was a clear primary local maximum of wind speed located at a radius of 40 km from the storm center extending up to a height of 5 km in both the observations and Edouard2. The vertical extension of the secondary wind speed maximum was also similar for the observations and Edouard2, although the secondary wind speed maximum was located further radially outward in the observations. There were clear primary and secondary maxima of radar reflectivity in both the observations and Edouard2, and these maxima were separated by a distinct moat region of weak or no convection. The secondary maximum of convection was co-located with the secondary wind speed maximum in Edouard2, consistent with conventional secondary eyewalls.

The evolution of azimuthal-mean radial-height structure of vertical velocity, total condensate, radial convergence, tangential winds, diabatic heating and cooling, and transverse circulation shown in Figure 14 confirms that the SEF in Edouard2 was governed by the same processes that led to the SEF in Idealized2 and Rita2. It was initiated from precipitation at the outer radii approximately 120–150 km from the storm center, evidenced by the downward extension of condensate. The forced lofting of the weak updraft in the area by the penetrative, evaporative cooling-driven downdraft promoted the development of local convection, evident from both the enhanced diabatic heating and updrafts. The convection-induced radial flow convergence served as an internal link to connect the convection and the boundary layer processes (Figures 14a–14d). Once the channel was established as the radial flow convergence extended down into the boundary layer (Figure 14e), it kicked off the positive feedback between convection and boundary layer processes that ultimately led to the rapid development of rainband convection and subsequent SEF in the manner that has been discussed in the previous sections (Figures 14e–14h). The inner and outer eyewalls are clearly defined by the maxima of updrafts, diabatic heating, and radial convergence. They are cleanly separated by a well-defined moat region, indicated by the downdrafts and diabatic cooling (green contours).

As shown in Figure 11, the vortex in Edouard1 underwent what on the first glance appeared to be a similar SEF to Edouard2, although the former was much less clean. A question that needs to be answered here is whether the two events resulted from the same physical processes. To clarify this issue, we applied the same analysis to Edouard1. Figure 15 shows the time evolution of azimuthal-mean radial-height structure of vertical velocity, total condensate, radial convergence, tangential winds, diabatic heating and cooling, and transverse circulation over the period that encompasses the entire life cycle of the ERC-like event in Edouard1. At 07 UTC 15 September, there was a precipitation event associated with a vertical velocity maximum centered at a radius approximately 170 km from the storm center (Figure 15a). In Edouard2, as well as Rita2 and Idealized2, we demonstrated that such a precipitation event at the farther radii triggered SEF. Apparently, it was not the case in Edouard1, as the precipitation event dissipated quickly, likely attributed to the much
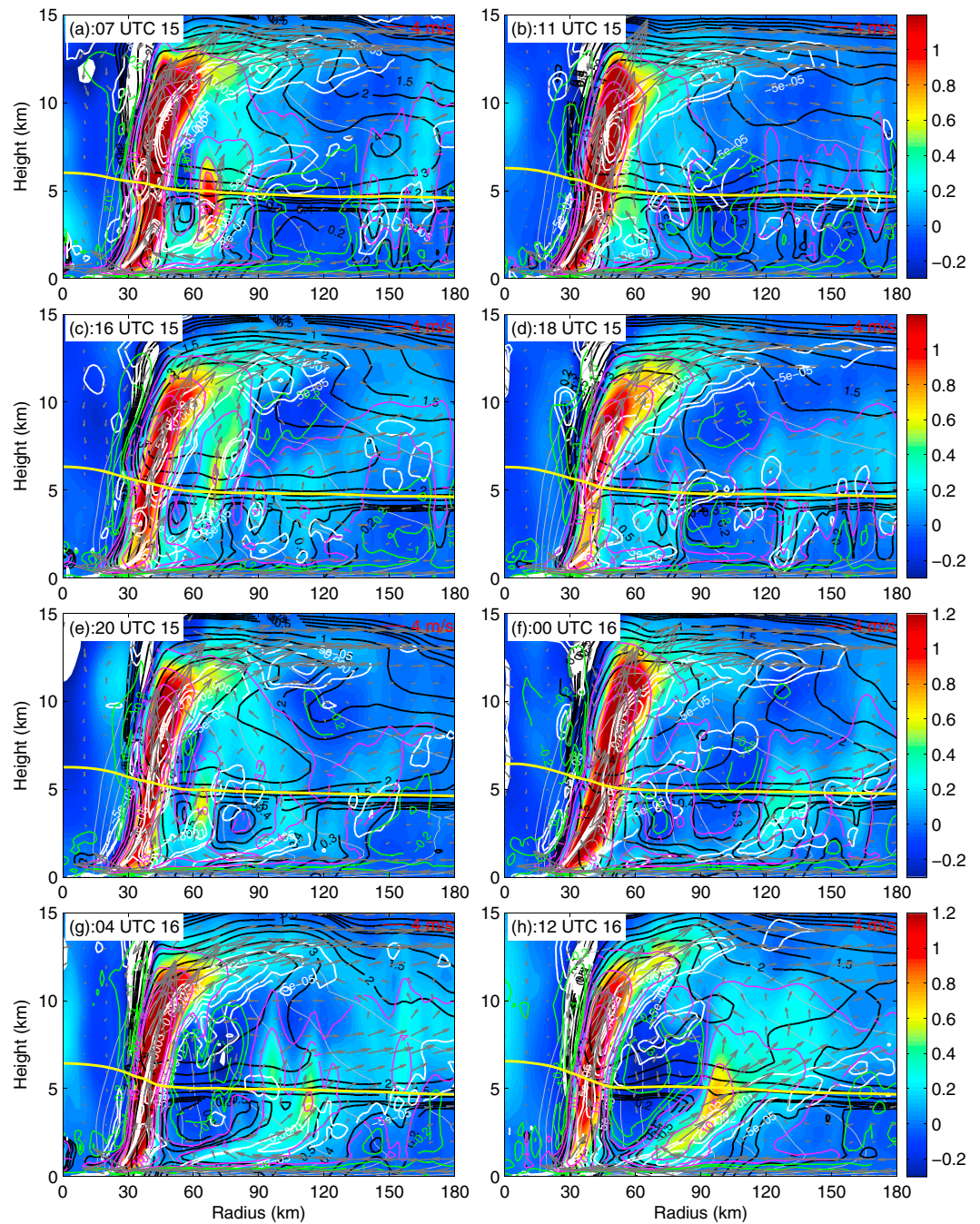
Figure 14. Radius-height cross section of azimuthally averaged vertical velocity (shading, m s^{-1}), total condensate (black contours, g kg^{-1}), radial convergence (white contours, s^{-1}), tangential winds (grey contours, m s^{-1}). diabatic heating (purple contours, K h^{-1}), diabatic cooling (green contours, K h^{-1}), and transverse circulation (vectors, m s^{-1}) for Edouard2. The yellow line denotes the freezing level.

smaller amount of condensate aloft than in Edouard2, and thus, the precipitation is merely transient (Figures 15b and 15c). This is in stark contrast to Edouard2 (Figure 14) in which the large amount of hydrometeor aloft supports the persistent precipitation in the outer rainband region. The inability to generate a long-lived precipitation event in Edouard1 prevented the persistent convective development in the outer rainband region, and thus, the positive feedback among precipitation, convection, and boundary layer processes was unable to be established in Edouard1. It is apparent that the SEF-like event in Edouard1 was not related to the hydrometeor fallout at the farther radii that triggered the SEF in
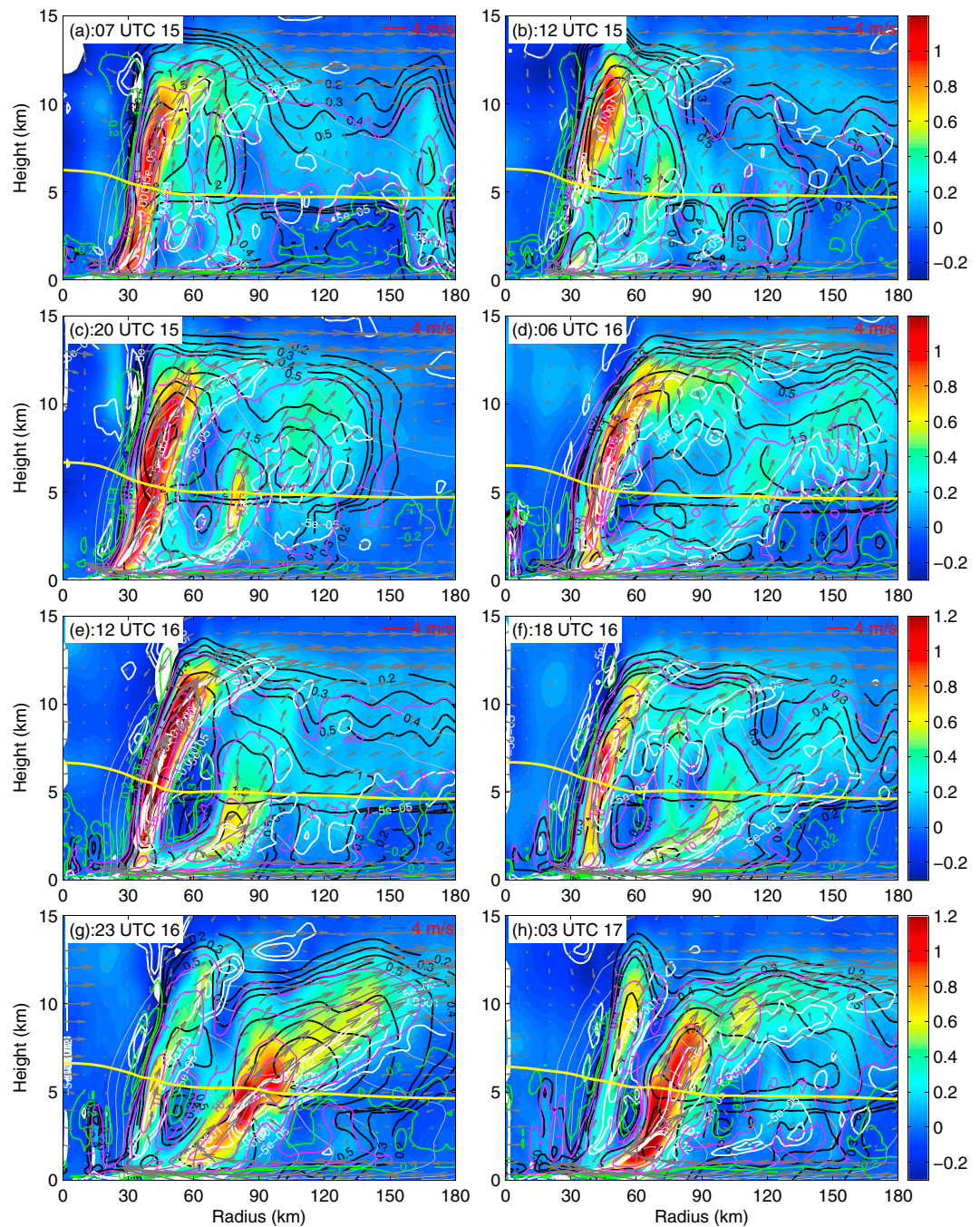
Figure 15. Radius-height cross section of azimuthally averaged vertical velocity (shading, m s^{-1}), total condensate (black contours, g kg^{-1}), radial convergence (white contours, s^{-1}), tangential winds (grey contours, m s^{-1}). diabatic heating (purple contours, K h^{-1}), diabatic cooling (green contours, K h^{-1}), and transverse circulation (vectors, m s^{-1}) for Edouard1. The yellow line denotes the freezing level.

Edouard2. This once again indicates the importance of radial transport and distribution of solid-phase hydrometeors in regulating vortex inner-core structure including SEF. To verify this important result, we performed a budget analysis of azimuthal-mean total condensate for the two simulations. For details of the derivation of the budget equation and procedure of performing budget analyses, please refer to Appendix A. Figure 16 compares the individual contributions of radial advection and vertical advection of total condensate by the vortex mean flow as well as the transport of condensate induced by the resolved eddies for Edouard1 and Edouard2, where the budget has been averaged over the same time periods as
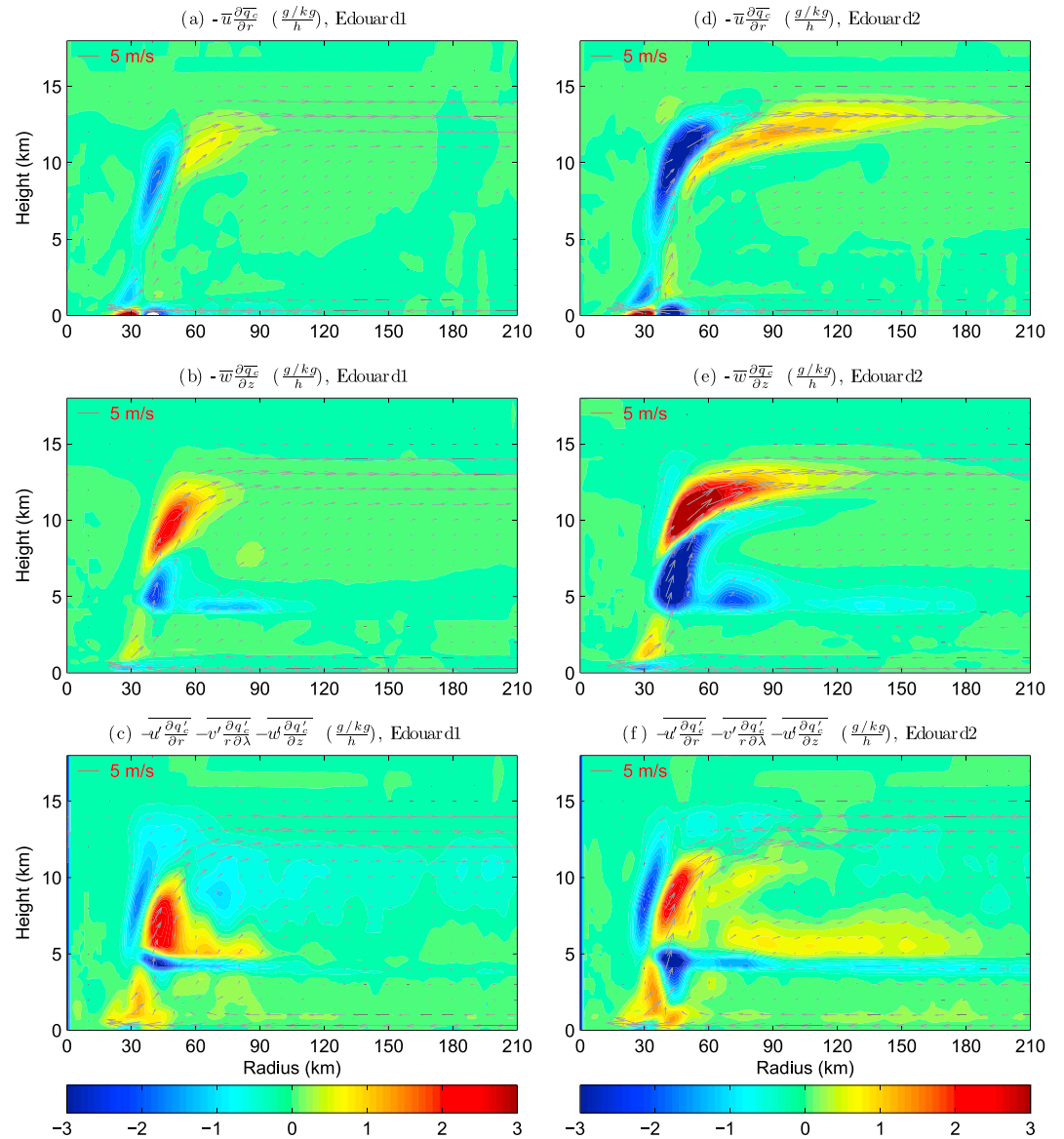
Figure 16. Azimuthal-mean total condensate budget analysis for (a–c) Edouard1 and (d–f) Edouard2. Plotted terms are radial advection by the vortex mean flow (g kg^{-1} hr^{-1}) (Figures 16a and 16d), vertical advection by the vortex mean flow (g kg^{-1} h^{-1}) (Figures 16b and 16e), and advection by the resolved eddies (g kg^{-1} h^{-1}) (Figures 16c and 16f).

in Figures 14 and 15. It clearly shows that the reduction of particle fall velocity in Edouard2 substantially increases the radial transport of condensate by the outflow (Figure 16d). It is this enhanced radially outward transport of condensate that supports the persistent precipitation at the farther outer radii, which promotes the local convection and initiates SEF. In contrast, the much weaker radial transport of condensate in Edouard1 is insufficient to maintain persistent precipitation in the outer rainband region. Although the transient precipitation may occur as was shown in Figure 15, it dissipated quickly and was unable to kick off the positive feedback leading to top-down SEF. In addition to the resultant change in radial transport of condensate, the reduction of particle fall velocity also induces changes in vertical advection and eddy transport of condensate. This is expected due to the interaction among processes. How vertical advection and eddy transport of condensate affect SEF remains unknown, as the signal is not as clean as the impact of radial transport. We leave this question for our future research.

Another important difference between Edouard1 and Edouard2 is the characteristics of the radial flow convergence located near the primary eyewall early in the simulations. In Edouard2, at 07 UTC 15 September, this

radial convergence was connected with the primary eyewall in the boundary layer and extended radially outward with height to approximately 120 km in radius and 7–8 km in altitude (Figure 14a). However, this radial convergence in Edouard2 quickly merged with the primary eyewall and had minimal connection with the region of radial convergence that developed after the development of steady precipitation at the outer radii (Figures 14b–14d). In Edouard1, the radial convergence near the primary eyewall was comparatively weaker at 0700 UTC 15 September than that in Edouard2, and it already resided in the boundary layer at this time (Figure 15a). This radial convergence never dissipated, but rather gradually strengthened as the TC vortex evolved. It eventually extended vertically upward, and ultimately resulted in the formation of a secondary eyewall (Figures 15b–15h). Compared to Edouard2, the secondary eyewall formed in Edouard1 was close to the primary eyewall, resulting in less clean separation by a moat downdraft.

In short, although they looked similar in appearance in Figure 11, the ERC events in Edouard1 and Edouard2 were fundamentally different, with the former emerging from existing radial flow convergence in the boundary layer in the near the outer rainband region via a bottom-up pathway and the latter from the hydrometeor fallout in the farther outer rainband region via a top-down pathway. The question is raised: what causes the longevity of the radial convergence near the primary eyewall in Edouard1, whereas it was only short lived in Edouard2? This may be related to the relative strengths of the primary eyewalls in the simulations. In Edouard2, the stronger primary eyewall exerted a hostile impact on the development of nearby secondary radial convergence, since compensating subsidence induced by the strong eyewall deep convection tends to limit the development of any nearby convection and promotes the development of a distinct moat downdraft. As a result, nearby rainband convection can be more readily absorbed by the primary eyewall. In contrast, the relatively weaker primary eyewall in Edouard1 might only have a limited impact on nearby rainband convection. As such, this nearby rainband convection may develop more freely to result in its longevity. On the flip side, the more active convection closer to the primary eyewall in Edouard1 weakened the primary eyewall by cutting off some of its low-level moist inflow. This also favors the longevity of radial convergence near the primary eyewall in Edouard1.

5. Discussion and Conclusions

Intense TCs often undergo one or more SEF and ERC events during their lifetimes, which can result in rapid changes in TC structure and intensity. In this study, we show HWRF's ability to produce SEF and an ensuing ERC is sensitive to the microphysical parameterization. An examination of simulated particle fall speed distributions reveals that the default HWRF Ferrier-Aligo scheme is not producing the smallest, lightest solid-phase hydrometeors with fall speeds less than 0.2 m s^{-1}. These lightest solid-phase hydrometeors, likely abundant in observed TCs, can be most easily lofted and transported to the outer radii and become the predecessor to SEF. We demonstrate that by reducing particle terminal velocity to a factor of one-fourth of the operational value, clean SEF occurred in both an idealized simulation and real-case simulations of Rita (2005) and Edouard (2014), which otherwise failed to occur in simulations with the default microphysics option due to a lack of particles with fall speeds less than 0.2 ms^{-1}.

Many features of the SEF in the real-case simulations of Rita2 and Edouard2 were consistent with the aircraft observations, including the timing of SEF, the secondary maximum in radial flow convergence, radial expansion of tangential winds, updrafts associated with the secondary eyewall, a well-defined moat region void of convection separating the primary and secondary eyewalls, and the radial-height structure of concentric eyewalls.

One of the major findings of our study is to reveal a top-down pathway to SEF. It is initiated from the emergence of steady precipitation at the outer radii. The forced lofting of the weak updraft in the area by the penetrative downdraft resulting from evaporative cooling promotes local rainband convection. The convection-induced radial flow convergence in this case serves as a mechanism to link the otherwise loosely connected mid-to-upper cloud processes and boundary layer processes. As the convergence extends down into the boundary layer, it triggers the eruption of high entropy air out of the boundary layer, leading to the rapid development of rainband convection and subsequent SEF via a positive feedback between precipitation, convection, and boundary layer processes. While the second part of this pathway to SEF is similar to what was described by Huang et al. (2012), who also emphasized the role of boundary layer radial flow convergence and near-surface tangential wind expansion in SEF, the emergence of radial flow convergence

above the boundary layer and its extension down into the boundary layer in our study is clearly not generated by boundary layer processes. This top-down pathway to SEF occurred in the sensitivity experiments with reduced particle fall velocity is in stark contrast to the SEF-like event in the control simulation of Edouard1, which was rooted in the boundary layer from the very beginning.

A key factor that governs the top-down pathway to SEF is the amount and radial distribution of solid-phase hydrometeors at the outer radii. A large amount of lofted hydrometeors at the outer radii advected from the primary eyewall in the anvil supports persistent precipitation there to result in a robust positive feedback among precipitation, convection, and boundary layer processes, leading to SEF in the simulations with reduced particle fall speed. In the case of the control simulations, the lack of abundant lofted hydrometeors at the outer radii may only lead to transient precipitation there and is thus insufficient to kick off the positive feedback required for SEF. The radial distribution of solid-phase hydrometeors is also important because of its control on the radial distance between the outer rainband convection and primary eyewall. A large radial distance between the outer rainband convection and primary eyewall allows for full development of moat downdrafts, which prevents the rainband convection moving inward and merging with the inner eyewall. This permits the rainband convection to develop freely and eventually result in clean concentric eyewalls.

While the top-down pathway to SEF is demonstrated here using sensitivity experiments with reduced particle fall speed, it is important to note that it is not appropriate to simply interpret the results as modulation of SEF by this fall speed. Rather, it fundamentally reflects the important control of SEF by the radial transport and distribution of solid-phase hydrometeors. Changing particle fall speed in this study is made only for the purpose of realizing different radial-height transport and distribution of hydrometeors, and thus, it should not be used as a means to tune microphysics. In our study, the reduction in particle fall speed allowed for the presence of the lightest solid-phase hydrometeors that were critical to SEF, but the universal reduction also led to the unrealistic removal of the larger solid-phase hydrometeors that are also likely present in real TCs. Nonetheless, the results presented in this study suggest that one of the causes for the failure of operational models to predict the observed SEF and ERC can be attributed to the incorrect simulation of radial transport and the resultant distribution of solid-phase condensate, which either fails to initiate the top-down pathway to SEF or generates unrealistic secondary-eyewall-like features too close to the primary eyewall.

In real TCs, microphysical processes directly interact with dynamical processes, such as convective updrafts/downdrafts and turbulent eddy circulations, to determine particle sedimentation. In numerical models, however, important SGS processes are handled by individual modules. How to generate a robust interaction among different modules in models to yield appropriate radial-height transport and distribution of hydrometeors is an important scientific issue that needs to be addressed. An improved representation of hydrometeor radial-height distribution of a vortex may substantially enhance HWRF's ability to predict TC intensity and structure change, including SEF and an ensuing ERC. In this regard, obtaining observations of detailed microphysical properties and the associated dynamic fields that can be used to validate the simulated microphysical and dynamic structure is critical.

Appendix A: Total Condensate Budget Analyses

The governing equation of total condensate in the cylindrical coordinate, where the coordinate origin is placed at the vortex center, may be written as

$$\frac{\partial q_c}{\partial t} + u\frac{\partial q_c}{\partial r} + v\frac{\partial q_c}{r\partial \lambda} + w\frac{\partial q_c}{\partial z} = Q_{c,\text{SGS}} + \dot{Q}, \tag{A1}$$

where r, λ, and z represent the radial, azimuthal, and vertical coordinates; u, v, and w are the radial, tangential, and vertical winds; and q_c is the total condensate. $Q_{c,\text{SGS}}$ and $\dot{Q}$ are the source/sink and subgrid scale (SGS) tendency of condensate, respectively. By decomposing the atmospheric field into the axisymmetric and asymmetric components, the azimuthal-mean total condensate budget equation may be written as

$$\underset{\text{(a)}}{\frac{\partial \overline{q}_c}{\partial t}} = \underset{\text{(b)}}{-\overline{u}\frac{\partial \overline{q}_c}{\partial r}} \underset{\text{(c)}}{-\overline{w}\frac{\partial \overline{q}_c}{\partial z}} - \underset{\text{(d)}}{\left(\overline{u'\frac{\partial q_c'}{\partial r}} + \overline{v'\frac{\partial q_c'}{r\partial \lambda}} + \overline{w'\frac{\partial q_c'}{\partial z}}\right)} + \underset{\text{(e)}}{\overline{Q_{c,\text{SGS}}}} + \underset{\text{(f)}}{\overline{Q}} \tag{A2}$$

where overbar and prime indicate the azimuthal mean and the perturbations from the azimuthal mean. Terms (a)–(f) indicate the local change, radial and vertical advection by the mean flow, transport by the

resolved eddies, SGS tendency, and local source of azimuthal-mean condensate, respectively. In this study, we calculated terms (a)–(d) using 5 min HWRF output. Terms (e) and (f) were indeterminable since some variables required for computing the terms are not available in the standard HWRF output. However, their contributions to condensate budget are presumably small because azimuthal-mean SGS processes are generally weak well above the boundary layer.

References

Abarca, S. F., & Corbosiero, K. L. (2011). Secondary eyewall formation in WRF simulations of Hurricanes Rita and Katrina (2005). *Geophysical Research Letters*, 38, L07802. https://doi.org/10.1029/2011GL047015

Abarca, S. F., Montgomery, M., Braun, S., & Dunion, J. (2016). Secondary eyewall dynamics as captured by an unprecedented array of GPS dropsondes deployed into Edouard 2014, 32nd Conference on Hurricanes and Tropical Meteorology, San Juan, PR., 19 April.

Abarca, S. F., & Montgomery, M. T. (2013). Essential dynamics of secondary eyewall formation. *Journal of the Atmospheric Sciences*, 70(10), 3216–3230.

Abarca, S. F., & Montgomery, M. T. (2014). Departures from axisymmetric balance dynamics during secondary eyewall formation. *Journal of the Atmospheric Sciences*, 71(10), 3723–3738.

Aligo, E., Ferrier, B., Rodgers, C., Pyle, M., Weiss, S., & Jirak, I. (2014). Modified microphysics for use in high resolution NAM forecasts, 27 AMS Conference on Severe Local Storms, Madison, WI., 7 November.

Bell, M. M., Montgomery, M. T., & Lee, W.-C. (2012). An axisymmetric view of concentric eyewall evolution in Hurricane Rita (2005). *Journal of the Atmospheric Sciences*, 69(8), 2414–2432.

Didlake, A. C. Jr., & Houze, R. A. Jr. (2011). Kinematics of the secondary eyewall observed in Hurricane Rita (2005). *Journal of the Atmospheric Sciences*, 68, 1620–1636.

Dunion, J. P., & Marron, C. S. (2008). A reexamination of the Jordan mean tropical sounding based on awareness of the Saharan air layer: Results from 2002. *Journal of Climate*, 21(20), 5242–5253.

Eliassen, A. (1951). Slow thermally or frictionally controlled meridional circulation in a circular vortex. *Astrophysica Norvegica*, 5, 19.

Fierro, A. O., Rogers, R. F., Marks, F. D., & Nolan, D. S. (2009). The impact of horizontal grid spacing on the microphysical and kinematic structures of strong tropical cyclones simulated with the WRF-ARW model. *Monthly Weather Review*, 137(11), 3717–3743.

Hawkins, J. D., & Helveston, M. (2008). Tropical cyclone multiple eyewall characteristics. Preprints. In *28th Conf. on Hurricanes and Tropical Meteorology*. Orlando, FL: American Meteorological Society. 14B.1.

Houze, R. A., Chen, S. S., Smull, B. F., Lee, W.-C., & Bell, M. M. (2007). Hurricane intensity and eyewall replacement. *Science*, 315, 1235.

Huang, Y.-H., Montgomery, M. T., & Wu, C.-C. (2012). Concentric eyewall formation in Typhoon Sinlaku (2008). Part II: Axisymmetric dynamical processes. *Journal of the Atmospheric Sciences*, 69(2), 662–674.

Judt, F., & Chen, S. S. (2010). Convectively generated potential vorticity in rainbands and formation of the secondary eyewall in Hurricane Rita of 2005. *Journal of the Atmospheric Sciences*, 67(11), 3581–3599.

Kepert, J. D. (2013). How does the boundary layer contribute to eyewall replacement cycles in axisymmetric tropical cyclones? *Journal of the Atmospheric Sciences*, 70(9), 2808–2830.

Kepert, J. D., & Nolan, D. S. (2014). Reply to comments on how does the boundary layer contribute to eyewall replacement cycles in axisymmetric tropical cyclones? *Journal of the Atmospheric Sciences*, 71, 4692–4704.

Kossin, J. P., & Sitkowski, M. (2009). An objective model for identifying secondary eyewall formation in hurricanes. *Monthly Weather Review*, 137, 876.

Locatelli, J., & Hobbs, P. (1974). Fall speeds and masses of solid precipitation particles. *Journal of Geophysical Research*, 79, 2185–2197. https://doi.org/10.1029/JC079i015p02185

Martinez, Y., Brunet, G., & Yau, M. (2010). On the dynamics of two-dimensional hurricane-like concentric rings vortex formation. *Journal of the Atmospheric Sciences*, 67(10), 3253–3268.

McFarquhar, G., & Black, R. (2004). Observations of particle size and phase in tropical cyclone: Implications for mesoscale modeling of microphysical processes. *Journal of the Atmospheric Sciences*, 61(4), 422–439.

Menelaou, K., Yau, M., & Martinez, Y. (2012). On the dynamics of the secondary eyewall genesis in Hurricane Wilma (2005). *Geophysical Research Letters*, 39, L04801. https://doi.org/10.1029/2011GL050699

Menelaou, K., Yau, M., & Martinez, Y. (2013). Impact of asymmetric dynamical processes on the structure and intensity change of two-dimensional hurricane-like annular vortices. *Journal of the Atmospheric Sciences*, 70(2), 559–582.

Menelaou, K., Yau, M., & Martinez, Y. (2014). Some aspects of the problem of secondary eyewall formation in idealized three-dimensional nonlinear simulations. *Journal of Advances in Modeling Earth Systems*, 6(3), 491–512.

Montgomery, M. T., Abarca, S. F., Smith, R. K., Wu, C.-C., & Huang, Y.-H. (2014). Comments on "How does the boundary layer contribute to eyewall replacement cycles in axisymmetric tropical cyclones?" *Journal of the Atmospheric Sciences*, 71, 4682–4691.

Montgomery, M. T., & Kallenbach, R. J. (1997). A theory for vortex rossby-waves and its application to spiral bands and intensity changes in hurricanes. *Quarterly Journal of the Royal Meteorological Society*, 123(538), 435–465.

Moon, Y., & Nolan, D. S. (2010). The dynamic response of the hurricane wind field to spiral rainband heating. *Journal of the Atmospheric Sciences*, 67(6), 1779–1805.

Nolan, D. S., Zhang, J. A., & Uhlhorn, E. W. (2014). On the limits of estimating the maximum wind speeds in hurricanes. *Monthly Weather Review*, 142, 2814–2837.

Qiu, X., & Tan, Z.-M. (2013). The roles of asymmetric inflow forcing induced by outer rainbands in tropical cyclone secondary eyewall formation. *Journal of the Atmospheric Sciences*, 70(3), 953–974.

Rozoff, C. M., Nolan, D. S., Kossin, J. P., Zhang, F., & Fang, J. (2012). The roles of an expanding wind field and inertial stability in tropical cyclone secondary eyewall formation. *Journal of the Atmospheric Sciences*, 69(9), 2621–2643.

Shapiro, L. J., & Willoughby, H. E. (1982). The response of balanced hurricanes to local sources of heat and momentum. *Journal of the Atmospheric Sciences*, 39(2), 378–394.

Tallapragada, V., Bernardet, L., Gopalakrishnan, S., Kwon, Y., Liu, Q., Marchok, T., … Zhang, X. (2015). Hurricane Weather Research and Forecasting (HWRF) model: 2015 scientific documentation, Developmental Testbed Center, 99.

Terwey, W. D., & Montgomery, M. T. (2008). Secondary eyewall formation in two idealized, full-physics modeled hurricanes. *Journal of Geophysical Research*, 113, D12112. https://doi.org/10.1029/2007JD008897

Wang, X., Ma, Y., & Davidson, N. E. (2013). Secondary eyewall formation and eyewall replacement cycles in a simulated hurricane: Effect of the net radial force in the hurricane boundary layer. *Journal of the Atmospheric Sciences*, *70*(5), 1317–1341.

Wang, Y. (2009). How do outer spiral rainbands affect tropical cyclone structure and intensity? *Journal of the Atmospheric Sciences*, *66*(5), 1250–1273.

Willoughby, H. E., Clos, J. A., & Shoreibah, M. G. (1982). Concentric eye walls, secondary wind maxima, and the evolution of the hurricane vortex. *Journal of the Atmospheric Sciences*, *39*, 395–411.

Zhang, F., Tao, D., Sun, Y. Q., & Kepert, J. (2016). Dynamics and predictability of secondary eyewall formation in sheared tropical cyclones. *Journal of Advances in Modeling Earth Systems*, *9*(1), 89–112.

Zhang, J. A., Nolan, D. S., Rogers, R. F., & Tallapragada, V. (2015). Evaluating the impact of improvements in the boundary layer parameterization on hurricane intensity and structure forecasts in HWRF. *Monthly Weather Review*, *143*, 3136–3155.

Zhang, J. A., Rogers, R. F., & Tallapragada, V. (2017). Impact of parameterized boundary layer structure on tropical cyclone rapid intensification forecasts in HWRF. *Monthly Weather Review*, *145*, 1413–1426.

Zhu, P., Zhu, Z., Gopalakrishnan, S., Black, R., Marks, F. D., Tallapragada, V., … Gao, C. (2015). Impact of subgrid-scale processes on eyewall replacement cycle of tropical cyclones in HWRF system. *Geophysical Research Letters*, *42*, 10,027–10,036. https://doi.org/10.1002/2015GL066436

Zhu, Z., & Zhu, P. (2014). The role of outer rainband convection in governing the eyewall replacement cycle in numerical simulations of tropical cyclones. *Journal of Geophysical Research: Atmospheres*, *119*, 8049–8072. https://doi.org/10.1002/2014JD021899

Zhu, Z., & Zhu, P. (2015). Sensitivities of eyewall replacement cycle to model physics, vortex structure, and background winds in numerical simulations of tropical cyclones. *Journal of Geophysical Research: Atmospheres*, *120*, 590–622. https://doi.org/10.1002/2014JD022056